This is a preprint, the final version is subject to change, of the American Mineralogist (MSA)
Cite as Authors (Year) Title. American Mineralogist, in press.
(DOI will not work until issue is live.) DOI: http://dx.doi.org/10.2138/am-2017-5631

Revision 3

Sperrylite saturation in magmatic sulfide melts: Implications for formation of PGE-bearing arsenides and sulfarsenides

Liping Bai [1], Sarah-Jane Barnes [1], Don R. Baker [2]

[1] Sciences de la Terre, Université du Québec a Chicoutimi, Québec G7H 2B1, Canada

[2] Earth and Planetary Sciences, McGill University, Montreal, Quebec, H3A 0E8, Canada

Abstract Sperrylite ($PtAs_2$) is one of most common Pt minerals, but the processes whereby it forms are not clearly established. Most commonly it is associated with the major-component base metal sulfide minerals (pyrrhotite, pentlandite and chalcopyrite), which are believed to have crystallized from magmatic sulfide melts. Hence, sperrylite is thought to have formed by crystallization from a sulfide melt or by exsolution from sulfide minerals. However, sperrylite is also found associated with silicate and oxide minerals where it is thought to have formed by crystallization from the silicate magma. In order to investigate the conditions under which sperrylite could crystallize from a magmatic sulfide melt we investigated sperrylite saturation in Fe-Ni-Cu-S sulfide melts under controlled fO_2 and fS_2 at 910-1060 °C and 1 bar. The As and Pt concentrations in the sulfide melt at sperrylite saturation increase from 0.23-0.41 wt% to 2.2-4.4 wt%, and from 0.36-0.65 wt% to 1.9-2.8 wt%, respectively, as the iron concentration in the sulfide melt decreases from 50 to 36 wt% at 910-1060 ºC. We show that transitional metal concentrations, particular iron and nickel, as well as sulfur and oxygen fugacities influence As and Pt concentrations in the sulfide melt at sperrylite saturation. These intensive variables appear to effect sperrylite solubility by influencing the oxidation state of As in the sulfide melt.

The measured concentrations of As and Pt in sperrylite-saturated sulfide melts produced in our experiments are much higher than that in most natural sulfides, implying that arsenides and sulfarsenides will not reach saturation in natural magmatic sulfide melts at high temperatures unless the magma has been contaminated with an exceptionally As-rich rock. This suggests that the observed arsenides and sulfarsenides in natural sulfide ores were not formed by crystallization from unfractionated sulfide melts at high temperatures above 900 °C, but might form at low temperatures below 900 °C.

INTRODUCTION

Arsenic is found to have a profound effect on the distribution of platinum group elements (PGE), because PGE have a stronger affinity for arsenides than for sulfides (Hanley, 2007; Piña et al., 2013). The highest PGE concentration (in particular Pt and Pd) is correlated with arsenide and sulfarsenide minerals in a number of sulfide deposits, such as the Platreef deposit in the Bushveld Complex (Holwell and McDonald, 2006), the Creighton Cu-Ni-PGE deposit in the Sudbury Igneous Complex, Canada (Dare et al., 2010), and the Aguablanca Ni-Cu-PGE deposit (SW Spain) (Piña et al., 2012a). In magmatic sulfide ore deposits, arsenides, sulfarsenides and other semimetal-bearing platinum group minerals (PGM) generally occur in four associations: (1) as mineral inclusions within base metal sulfides (BMS) (Barnes et al., 2008; Dare et al., 2010); (2) at grain boundaries of sulfides and silicates (Hanley, 2007; Barkov et al., 2009); (3) interspersed among the silicate grains (Barnes et al., 2008; Barnes et al., 2016); and (4) within oxides (Farrow and Watkinson, 1997). These textures are widely used to infer the PGM formation mechanisms (Naldrett, 1969; Gervilla et al., 1998; Li et al., 2008; Godel et al., 2012;

Piña et al., 2012a; Prichard et al., 2013; Canali and Brenan, 2015; Maier et al., 2015). However, textural information is not enough to infer the formation mechanism of arsenides and sulfarsenides because these phases can form either at high or low temperatures. It has been suggested that PGE-bearing arsenides and sulfarsenides form by early crystallization from a magmatic sulfide melt at high temperatures of 900-1200 °C (Hutchinson and McDonald, 2008; Dare et al., 2010), by crystallization from a silicate melt (Maier et al., 2015; Barnes et al., 2016), or by crystallization from an immiscible arsenide melt at high temperatures (Hanley et al., 2007; Piña et al., 2013). If these processes occur before the first sulfide mineral crystallizes, the As-rich melt or PGM arsenides and sulfarsenides could collect most PGE and other trace metals that have an affinity for As. If these crystals are then removed from the system (e.g., by fractional crystallization), the residual magma can become depleted in PGE (Dare et al., 2010; Piña et al., 2012b).

However, the distributions of PGE in some deposits suggest that PGE-bearing arsenides and sulfarsenides can also form at low temperatures by two different processes: (1) by direct exsolution of Pt and Pd along with As that were are initially dissolved in base metal sulfides (BMS) to form As-bearing PGM at temperatures probably below 500 °C (Barnes et al., 2008; Piña et al., 2012a); or (2) by crystallization from an immiscible arsenide melt that segregated from the sulfide melt after sulfide crystallization had begun (Hanley, 2007; Holwell and McDonald, 2007). In the first case, PGE, As and other semimetals remain dissolved in BMS during sulfide crystallization at high temperatures, but exsolve from BMS during subsequent cooling, so most PGMs are distributed within rather than around the BMS grains. Also, they can

have rounded and lath-shaped morphologies associated with slow cooling (Piña et al., 2012a). In the second case, the compatible elements such as Ir will have partitioned into the early formed sulfides, leaving the fractionated, residual sulfide liquid enriched in Pt and Pd relative to intermediate PGM such as Ir. These incompatible elements will finally crystallize from an immiscible arsenide melt to form various Pt- and Pd-bearing PGMs (Fleet et al., 2003; Holwell and McDonald, 2010). These PGMs are not only distributed as inclusions in base metal arsenides and sulfarsenides, but may also be distributed around the BMS grains (Tomkins, 2010; Piña et al., 2012a). These PGMs generally have euhedral to anhedral morphologies (Hanley, 2007).

Whether arsenides and sulfarsenides form at high or low temperatures depends upon when As-bearing phases reach saturation in a magmatic sulfide melt. The solubility of arsenide and sulfarsenide phases determine the timing and sequence of the crystallization of arsenide phases in which these elements are essential structural constituents. Although experiments have investigated the partitioning of As and the influence of As on the behavior of noble metal species in magmatic sulfide melts (Helmy et al., 2010, 2013b; Sinyakova and Kosyakov, 2012; Canali and Mungall, 2015; Liu and Brenan, 2015), the data for As concentrations in magmatic sulfide melts is limited. Helmy et al. (2013a) investigated the As and Pt concentrations in magmatic sulfide melts saturated with sperrylite and demonstrated that the As and Pt concentrations are strongly dependent on temperature, varying from 0.02 to 1.5 wt% and 0.14 to 1.5 wt%, respectively, at 700-1230 °C in the system investigated. However, the bulk compositions of the experiments was kept constant and fO_2 and fS_2 were not controlled in the Helmy et al. (2013a) study. Additional studies are needed because sulfur and iron concentrations in magmatic sulfide

ores vary (Ebel and Naldrett, 1996), and Pt solubility in sulfide melts is strongly influenced by the fO_2 and fS_2 (Pruseth and Palme et al., 2004; Fonseca et al., 2009). To better understand sperrylite saturation in sulfide melts, we performed experiments with 4 different bulk compositions containing Fe, Ni, Cu and S at concentrations similar to those in nature under controlled fO_2 and fS_2 similar to natural conditions at 910-1060 °C and 1 bar.

EXPERIMENTAL AND ANALYTICAL METHODS

Experimental methods

Four Fe-Ni-Cu-S starting materials for the experiments were synthesized using mixtures of high purity metals and sulfur powder (Alfa Aesar 99.999% Cu, 99.998% Fe, 99.996% Ni, 99.999% S). The copper and nickel concentrations in the starting materials were held approximately constant while the iron/sulfur ratio varied, resulting in a set of starting materials with sulfur concentrations from 36 to 43 wt% and Fe concentrations from 49 to 41 wt% (Table 1). The mixtures were synthesized in evacuated silica tubes heated at 1000-1100 °C for 1 hour to 2 days, depending on the sulfur content.

In our experiments the fO_2 was controlled by the Fayalite-Quartz-Magnetite (FMQ) buffer. The fayalite was synthesized from quartz (Alfa Aesar 99.99%) and hematite (Alfa Aesar 99.9995%) at 1 bar using a gas mixing furnace. The fS_2 was controlled by the platinum-cooperite (Pt-PtS) buffer. The cooperite was synthesized from pure Pt (Alfa Aesar 99.98%) and sulfur powder at 1 bar. The fO_2 and fS_2 for each experiment were calculated using thermochemical data from Barin (1995).

The experimental capsule is shown in Figure 1. Sperrylite was added as $PtAs_2$ crystals that were from either the Vermilion mine or the Broken Hammer occurrence, both associated with the Sudbury Igneous Complex, Canada. Generally 200-400 mg of the sulfide mixture and a chip of $PtAs_2$ crystal were loaded into silica tubes of 6 mm in OD. The sulfide mixture was covered by a silica powder layer of 3-5 mm in thickness, which separated the sulfide from the FMQ buffer placed on the top of the silica layer. A small silica cup filled with the Pt-PtS buffer sat on the top of FMQ buffer. The loaded capsule tube was evacuated and sealed under vacuum. The final capsule was about 5-7 cm in length corresponding to the length of minimum temperature gradient in the furnace.

The temperatures were measured with a type-K sheathed thermocouple. The thermocouple tip was positioned close to the center of the capsule. The temperature was calibrated with a similar thermocouple. Our calibrations indicated that the temperature gradient for a capsule of 5-7 cm in length was within 3 °C.

The experiments were initially heated at 750 °C for 12 hours, then raised to the desired experimental temperatures (Table 1). After run durations for 12-186 hours, the experiments were quenched by dropping the capsules into cold water. The run products along with FMQ and Pt-PtS buffers were mounted in epoxy for analysis.

Analytical methods

132 The concentrations of Fe, Ni, Cu, S, As and Pt in the run products were analyzed using laser
133 ablation inductively-coupled plasma mass spectrometry (LA-ICP-MS) at LabMaTer in the
134 University of Quebec at Chicoutimi (UQAC), Canada. The LA-ICP-MS analysis was performed
135 using line scans with a beam size of 20 μm, a laser frequency of 15 Hz, a power of 5 mJ/pulse,
136 and a stage speed of 5 μm/s. The internal standard used was ^{34}S determined from the sulfur
137 concentration measured by electron microprobe at McGill University. The isotopes monitored
138 were ^{33}S, ^{34}S, ^{57}Fe, ^{60}Ni, ^{61}Ni, ^{63}Cu, ^{65}Cu, ^{75}As, ^{195}Pt, and ^{196}Pt. The isotopes used to determine
139 the elemental concentrations were ^{33}S, ^{34}S, ^{57}Fe, ^{60}Ni, ^{63}Cu, ^{75}As, and ^{195}Pt. The Pt, Fe and S
140 were calibrated with Po-727, a FeS doped with ~ 40 ppm PGE supplied by Memorial University.
141 Cu and As were calibrated with Mass-1, a FeCuZnS pressed pellet doped with ~ 50 to 100 ppm
142 trace elements supplied by the USGS. Ni was calibrated with MASS-3 and NiS pressed pellets
143 also provided by USGS. JB-MSS-5, a FeS doped with 50-1000 ppm trace elements supplied by
144 Prof J. Brenan, University of Toronto, was used to monitor the calibration. A total 3 to 22 laser
145 traverse lines across quenched sulfide melts or equilibrium *mss* were analyzed for each sample.
146 Data reduction was performed with Iolite software. The average and standard derivations of the
147 concentrations of each element based upon multiple analyses are listed in Table 1.
148
149 The electron microprobe analysis used a beam size of 3 μm and a beam current of 100 nA. The
150 accelerating voltage was 20 kV. The counting time was 240 s. The major elements Fe, Ni, Cu
151 and S were analyzed for 20 s on the X-ray peak and 10 s on each background, whereas As and Pt
152 were analyzed for 60 s on the peak and 30 s on each background. The standards were the Canmet
153 sulfide standard and the Astimex metal standard.

154 The quenched sulfide melts primarily consist of quenched *mss* (q-*mss*), quenched *iss* (q-*iss*),
155 quenched base metal sulfide liquids rich in As and Pt (q-BMS), and quench $PtAs_2$ crystals (q-
156 $PtAs_2$). Quench As droplets were also found in some experiments. The internal standard S
157 concentrations used for LA-ICP-MS analysis of the quenched sulfide melts were determined by
158 integration based on following equation:

159 $$C^S(wt\%)=C^S_{q-mss}\phi_{q-mss}\times\frac{\rho_{q-mss}}{\rho_{sul}}+C^S_{q-iss}\phi_{q-iss}\times\frac{\rho_{q-iss}}{\rho_{sul}}+C^S_{BMS-l}\phi_{BMS-l}\times\frac{\rho_{BMS-l}}{\rho_{sul}}+C^S_{q-PtAs_2}\phi_{q-PtAs_2}\times\frac{\rho_{q-PtAs_2}}{\rho_{sul}} \quad (1)$$

160 where C^S_{q-mss}, C^S_{q-iss}, C^S_{BMS-l}, $C^S_{q-PtAs_2}$ are the S concentrations (wt%) in q-*mss*, q-*iss*, q-BMS
161 liquid and q-$PtAs_2$ analyzed by electron microprobe analysis. Note the S concentration in q-
162 $PtAs_2$ crystals is caused by the interference from the surrounding matrix because most q-$PtAs_2$
163 crystals were extremely small (~ 0.1 to 1 μm). ϕ_{q-mss}, ϕ_{q-iss}, ϕ_{BMS-l}, ϕ_{q-PtAs_2} are the volume
164 fractions of q-*mss*, q-*iss*, q-BMS liquid and q-$PtAs_2$ in sulfide melt ($\phi_{q-mss}=\frac{V_{q-mss}}{V_{sul}}$, $\phi_{q-iss}=\frac{V_{q-iss}}{V_{sul}}$
165 , $\phi_{BMS-l}=\frac{V_{BMS-l}}{V_{sul}}$, $\phi_{q-PtAs_2}=\frac{V_{q-PtAs_2}}{V_{sul}}$); they were determined by image analysis on backscattered
166 images using the ImageJ program (Rasband, 2005). V_{sul} is the volume of sulfide melt. ρ_{sul} is the
167 density of sulfide melt, close to 4-4.5 g cm^{-3} (Mungall and Su, 2005; Kress et al., 2008).
168 Mungall and Su (2005) found that the density of sulfide melt is not dependent on Cu or Ni
169 content, thus we consider that the density of q-*mss* or q-*iss* is similar to sulfide melt (i.e.,
170 $\frac{\rho_{q-mss}}{\rho_{sul}}\approx 1, \frac{\rho_{q-iss}}{\rho_{sul}}\approx 1$). The density of q-BMS liquid, ρ_{BMS-l}, is similar to ρ_{q-iss}, because Fe, Ni
171 and Cu concentrations in q-BMS liquid are similar to that in q-*iss*, except that q-BMS liquid has
172 higher As and Pt concentrations of 3-9.8 wt%, which are not expected to cause a significant

difference in density between q-BMS liquid and q-*iss*. The density of q-$PtAs_2$, ρ_{q-PtAs_2}, is 10.38 g cm^{-3}. Note that for samples containing As droplets, we integrated them together with q-$PtAs_2$ crystals because it is hard to discriminate them from q-$PtAs_2$ by image analysis.

We also studied the textures of these run products with a field emission scanning electron microscope at the University of Montreal.

EXPERIMENTAL RESULTS

Texture of equilibrium crystals

Residual sperrylite crystals were present at the end of all runs except SPT3 and SPT5. SPT3 and SPT5 were initially loaded with smaller sperrylite crystals, which completely dissolved into the sulfides during the experiments.

Equilibrium *mss* crystals were found in all experiments except SPT16, 17, 20 and 21 that were performed at higher temperatures, above the stability of equilibrium *mss* in the studied bulk compositions. Both LA-ICP-MS and microprobe analyses show no compositional variations among equilibrium *mss* in each experiment, consistent with the achievement of equilibrium. Most equilibrium *mss* are sub-rounded to rounded (Fig. 2a), varying from 100 to 500 μm in size.

Texture of quench crystals

Most quenched sulfide melts contain intergrowths of q-*mss* and q-*iss*, 5 to 20 μm in size (Fig. 2b). Between the q-*mss* and q-*iss* are fine elongate quenched crystals approximately <1 μm wide

and 2 μm long; they have a similar composition to q-*iss* except they contain 1.1-5.8 wt% As and Pt, and probably represent the residual BMS liquid after the crystallization of q-*mss* and q-*iss* (Fig. 2b). Quench $PtAs_2$ crystals occurred in all these experiments. They are irregular, skeletal, or dendritic (Fig. 2b, c, d), and distributed along the boundary of q-*mss*, within q-*iss*, within q-BMS liquid, or within As droplets. There is a significant difference in the size of these crystals. The quench $PtAs_2$ crystals distributed within q-BMS liquid can be up to ~ 5-13 μm in size (Fig. 2b, c), in contrast to those of ~ 0.1-1 μm in size distributed along the boundary of q-*mss*, within q-*iss* or within As droplets (Fig. 2d). The textural relations suggest that they crystallized after q-*mss*, q-*iss* and q-BMS liquid. Most of these quench crystals are too small to analyze, but analysis of some larger crystals display As:Pt atomic ratios close to 2, thus we identified them as $PtAs_2$ crystals. Some Cu, Fe, Ni, or S are also detected in the compositions of $PtAs_2$ crystals (Table 2), but this could be interference from the surrounding matrix.

Texture of As droplets

Many As droplets were found in quenched sulfide melts, as illustrated by As spectra signals from LA-ICP-MS and also confirmed by SEM imaging. Most As droplets occurred in experiments with high iron concentration (bulk 36-38 wt% S and 44-49 wt% Fe) except SPT12 and SPT14, which were performed for 12 and 24 h, respectively, as opposed to the other experiments with durations greater than 24 h. The As droplets occur as sub-spherical to spherical globules. There is a significant difference in the size of these As droplets. They vary from ~ 0.25 to 2 μm in diameter in low temperature experiments (≤ 1000 °C) (Fig. 2b, d), but in higher temperature experiments (1060 °C), the As droplets can be up to ~ 11 μm in diameter. The As droplets in

backscattered images appear dark-grey with skeletal to dendritic bright crystals inside (Fig. 2d). EDS analyses show that the dark-grey matrix is rich in As, and the exsolved bright crystals are rich in Pt; however, they are too small to allow the composition of each phase to be determined. Electron microprobe analysis can only give the composition of the whole As droplets, showing they are rich in As, Pt, and Ni, but depleted in Fe (~ 3.1-7.2 wt%) and S (< 0.3 wt%) (Table 2). The observed textures in these experiments are similar to those found by Helmy et al. (2013a) in their study of sperrylite stability in a sulfide melt with a bulk sulfur composition of 35.8 wt%. To verify if these drop-like arsenides represent an immiscible arsenide melt formed at 910-1060 ºC in our experiments, thermodynamic calculations were performed with Factsage (Bale et al., 2009) using the FTmisc database which contains the optimized parameters for the Fe-Cu-Ni-Co-Cr-As-S system. The calculations predict that only one sulfide melt phase is present at equilibrium, and that no immiscible arsenide melt should form. This is unlike Helmy et al's (2013a) results in the Pd-bearing, but Pt-free sulfide system, where an immiscible arsenide melt was observed.

BASE METAL, A_S AND Pt DISTRIBUTION IN SULFIDE MELT AND EQUILIBRIUM *MSS*

Equilibrium of the experiments

Two lines of evidence indicate that the dissolution of $PtAs_2$ in sulfides achieved equilibrium in our experiments:

(1) The major element concentrations in the sulfide melt from isothermal experiments of short (12.4 h) and medium (24 h) duration are within the uncertainties of each other (Table 1). This is

239 shown by two of our lowest temperature experiments at 930 ºC in Figure 3. These durations are
240 similar to those of Pruseth and Palme (2004), which demonstrated that Fe, S and Pt can reach
241 equilibrium within 2 to 72 hours;
242 (2) The partition coefficients of Cu, Fe, As and Pt between equilibrium *mss* and sulfide melt are
243 not dependent on equilibrium *mss* compositions. The partition coefficient of Cu between
244 equilibrium *mss* and melt ($D_{Cu}^{mss/melt}$) from our experiments has an average value of 0.22 ± 0.03,
245 very close to that found in previous As-bearing experiments (Sinyakova and Kosyakov, 2012;
246 Helmy et al., 2010, 2013a). The relation of $D_{Cu}^{mss/melt}$ and sulfur in equilibrium *mss* (i.e., at.% S in
247 equilibrium *mss*) shows that $D_{Cu}^{mss/melt}$ in our experiments does not vary with at.% S in equilibrium
248 *mss* over the at.% S range of 49.8 to 52.6, consistent with the results found in previous As-
249 bearing experiments (Helmy et al., 2010, 2013a; Sinyakova and Kosyakov, 2012). Similarly,
250 $D_{Fe}^{mss/melt}$, $D_{Pt}^{mss/melt}$ and $D_{As}^{mss/melt}$ in our experiments also do not vary with at.% S in equilibrium
251 *mss*, implying that the partition coefficients of these elements are independent of equilibrium *mss*
252 composition (manuscript in preparation). $D_{Ni}^{mss/melt}$ in our experiments varies over a wide range of
253 0.91-2.64; there is not a correlation between $D_{Ni}^{mss/melt}$ and at.% S in equilibrium *mss*, similar to
254 that found in Helmy et al.'s experiments (2013a).
255
256 **Base metal distribution**
257 The compositions of quenched sulfide melts and equilibrium *mss* are listed in Table 1. The LA-
258 ICP-MS analyses reveal major element homogeneity in both melt and equilibrium *mss*. Such
259 results are also confirmed by measurements from microprobe analyses. The differences between
260 the major element concentrations in the melt measured by LA-ICP-MS and microprobe are

minor, within 2.8% relative; this difference is less than the uncertainty for the analyses. The LA-ICP-MS analyses give the integrated composition of quenched sulfide melts, showing they are rich in Cu, varying from 9.1 to 31 wt%, and depleted in Ni, varying from 2.9 to 6.8 wt%. Cu concentrations in the sulfide melt from experiments with similar bulk sulfur increase as temperature drops. The high Cu contents (up to 21-31 wt%) measured in our fractionated sulfide melts are consistent with those found in natural Ni-Cu sulfide ore deposits (Barnes and Lightfoot, 2005) and experimentally produced sulfide melts (Ebel and Naldrett, 1996; Mungall et al., 2005; Helmy et al., 2013a). In contrast to the melt, the equilibrium *mss* is rich in Ni and depleted in Cu (Table 1). Ni concentration in equilibrium *mss* varies from 5.8 to 9.2 wt%, and Cu varies from 4.7 to 7.5 wt%.

As and Pt distribution in sperrylite-saturated sulfide melts

The As and Pt concentrations in sulfide melts show a strong dependence on temperature and iron concentration in the melt (Fig. 4a, b). The As and Pt concentrations in sulfide melts at sperrylite saturation are inversely correlated with the temperature and the Fe concentration in the melt. The higher the iron concentration in the melt and the lower the temperature, the lower the As and Pt concentrations at sperrylite saturation. The highest concentrations of As and Pt in sperrylite-saturated melts are found in the melt with low iron concentration (Fig. 4a, b). For example, at ~ 1000 °C, the sulfide melt with 38 wt% Fe requires ~ 40 000 ppm As and ~ 35 000 ppm Pt to achieve sperrylite saturation, whereas the sulfide melt with 50 wt% Fe needs only ~ 2 000 ppm As and ~ 4 000 ppm Pt to achieve sperrylite saturation (Fig. 4a, b).

As and Pt distribution in equilibrium *mss*

The As and Pt concentrations in equilibrium *mss* saturated with sperrylite do not show a clearly discernable dependence upon temperature, but are weakly sensitive to the iron concentrations (Fig. 4c, d). The concentration of As in sperrylite-saturated *mss* only varies from ~ 135 to 300 ppm and that of Pt from ~ 1 800 to 4 000 ppm, or approximately a factor of two in each case.

DISCUSSION

Dissolution reaction for sperrylite

The molar concentrations (moles per 100 g of sulfide melt) of As versus Pt in the sulfide melt produced in *mss*-free experiments performed at 1060 and 1000 °C follow a linear trend with a slope of ~ 2 (Fig. 5), indicating that sperrylite dissolution can be described by the reaction:

$$PtAs_2^{\text{sperrylite}} \leftrightarrow Pt^{\text{sulfide liquid}} + 2\ As^{\text{sulfide liquid}} \quad (2a)$$

The slope of ~ 2 indicates that all of the platinum and arsenic released by sperrylite dissolution is dissolving into the sulfide melt and that no other phases are preferentially removing either Pt or As.

However, the concentrations of Pt in *mss*-saturated experiments at 980 and 1005 °C are displaced to lower values than predicted by the fit to the 1000 °C experiments (Fig. 5), even though the Pt concentrations in our 980 and 1005 °C experiments are consistent with the As versus Fe trend in the 1000 °C experiments in Figure 4a. Furthermore, the *mss*-saturated experiment of Helmy et al. (2013a) at 1000 °C displays a similar Pt depletion when compared to our results (Fig. 5), whereas the results of a *mss*-free experiment of Helmy et al. (2013a) at 1050 °C contains Pt and

As concentrations consistent with the reaction above (Fig. 5). This displacement of Pt concentrations to lower values in *mss*-saturated experiments is attributed its incorporation into equilibrium *mss* (Table 1). We note that the Pt concentrations in our experimental sulfide melts, which vary from 0.38 to 3.23 wt% at log fO_2 of -11 to -13.7 and log fS_2 of -2.2 to -3.6, are similar to previous measurements in Pt-saturated sulfide melts at 1200-1300 °C with ~ 0.32 to 3.1 wt% Pt at log fO_2 of -10.9 to -14.9 and log fS_2 of -2.2 to -3.64 (Fonseca et al., 2009).

Oxidation state of arsenic in the sulfide melt

The formal oxidation state of Pt in sperrylite is 4^+ and that of As is 2^-, but the oxidation state of As in the sulfide melt may be different. Helmy et al. (2010) argue that some of the arsenic dissolved in the sulfide melt is oxidized at sulfur fugacities similar to those in this study (log fS_2 ~ -3). The oxidized arsenic cations will not replace sulfur in the sulfide melt, but may react with S to form AsS and As_2S_3 species (Helmy et al., 2013a).

To better understand the effects of the As oxidation state on sperrylite dissolution we consider the following reactions describing the behavior of As during dissolution of sperrylite and oxidation of the dissolved arsenic to a cation of unspecified positive charge, n:

$$PtAs_2^{\text{sperrylite}} \leftrightarrow Pt^{4+,\ \text{sulfide liquid}} + 2\ As^{2-,\ \text{sulfide liquid}} \qquad (2b)$$

and

$$As^{2-,\text{sulfide liquid}} \leftrightarrow As^{n+,\ \text{sulfide liquid}} + (2+n)\ e^- \quad . \qquad (3)$$

The oxidation of As^{2-} to As^{n+} will reduce the concentration and activity of As^{2-} in the sulfide melt, and therefore influence the solubility of sperrylite. As the ratio of oxidized to reduced arsenic in the melt increases, so does the concentration of total arsenic in the melt required to achieve sperrylite saturation. In addition, the electrons released by arsenic oxidation become available for the reduction of other ions in the system.

Many intensive variables in addition to fS_2 will affect the oxidation state of arsenic. Obviously, the oxygen fugacity will have an effect, and the sulfide melt at oxygen and sulfur fugacities similar to those used in this study is known to contain oxygen at weight percent concentration levels (e.g., Kress, 1997; Mungall et al., 2005). Additionally, the concentrations of other heterovalent cations in the sulfide melt may affect the oxidation of arsenic. The abundance of transition metals in the sulfide melt, particularly iron and the observation that it exists in both ferric and ferrous states in the sulfide melt (Kress, 1997), suggests that they may play an important role in influencing the oxidation state of arsenic.

Effect of iron

The relationships between As and Fe concentrations and Pt and Fe concentrations in the sulfide melt at sperrylite saturation shown in Figures 4a and 4b provide evidence that higher iron concentrations in the sulfide melt result in lower sperrylite solubilities at the buffered fO_2 and fS_2 of our experiments. We attribute the higher sperrylite solubilities observed in the sulfide melt with lower iron concentrations to its relatively higher concentrations of oxygen and ferric iron compared to the sulfide melt with higher iron concentrations. This hypothesis is based upon the

data of Kress (1997) that demonstrate that an increase in the iron concentration of the sulfide melt results in a decrease in oxygen concentration at constant fO_2 and fS_2, which can be associated with ferric iron in the sulfide melt.

Figure 4 demonstrates that, at similar temperatures, the concentration of As and Fe in sperrylite-saturated sulfide melts are approximately 8x greater than those measured by Helmy et al. (2013a) at similar temperatures and iron concentrations. We attribute the differences between our measurements of sperrylite solubility and those of Helmy et al. (2013a) shown in Figure 4 to a combination of differences in fO_2, fS_2, and transition metal concentrations in the two studies. The oxygen fugacity of Helmy et al.'s (2013a) experiments was not constrained, but the fS_2 estimated from the composition of the *mss* was log fS_2~ -5, or approximately 2 log units below our study (Table 1) and at conditions where dissolved arsenic is dominated by the anionic species (Helmy et al., 2010). And, while the iron concentrations in the sulfide melts produced in the experiments of Helmy et al. (2013a) and this study are similar, the nickel concentrations in Helmy et al.'s melts varied from 16.8 to 23.4 wt.%, whereas in our melts they were only 3.5 to 9.5 wt%.

The sperrylite solubility measurements in this study can be analyzed in a van't Hoff diagram in which the measured solubility product, $X_{Pt}X_{As}^2$ (based upon Equation 2a) versus 10 000/T is plotted (Fig. 6). The solubility data for melts with low $X_{Fe}/(X_{Fe}+X_S)$, from 0.356 to 0.370, form a linear trend with a slope that yields an enthalpy of reaction of 5.42 ± 2.90 kJ and with an intercept of 24.0 ± 20.0 (Fig. 6). Although the uncertainty of the enthalpy of the reaction is large

368 because of the few data points used for its calculation, it still provides a useful reference for
369 understanding the trends seen our measurements of the sperrylite solubility data.
370
371 Traditionally the intercept of a line on a van't Hoff diagram is equated with the entropy of the
372 reaction:

373 $$\ln K = (-\Delta H^o/R)\,(1/T) + \Delta S^o/R \quad . \qquad (4)$$

374 However, splitting the equilibrium constant into separate terms for the concentration and for the
375 activity coefficients, γ, for Equation 2a leads to the following form

376 $$\ln (X_{Pt}X_{As}^2) = (-\Delta H^o/R)\,(1/T) + \Delta S^o/R \; - \; \ln (\gamma_{Pt}\gamma_{As}^2). \qquad (5)$$

377 In this formulation of the van't Hoff equation the intercept identified for the sulfide melt with
378 low iron concentrations corresponds to the sum of the entropy term and the activity coefficient
379 term. Assuming constant ΔH^o (i.e., constant slope), the two most iron-rich melts, $X_{Fe}/(X_{Fe}+X_S)$
380 of 0.458 and 0.466, were fit with the van't Hoff equation by changing only the intercept to a
381 value of 15.3 (Fig. 6). Given constant ΔS^o, the significant difference between the intercept values
382 at high and low iron concentrations reflects a change in the $\ln(\gamma_{Pt}\gamma_{As}^2)$ term from the iron-rich to
383 the iron-poor melts. Figure 6 is also contoured with other lines at constant slope for comparison
384 with the melt compositions at intermediate values of $X_{Fe}/(X_{Fe}+X_S)$. Of our three data points that
385 plot in this intermediate region, two are consistent with an increase in the activity coefficient
386 term as the $X_{Fe}/(X_{Fe}+X_S)$ value of the melt drops (Fig. 6). The third does not does not (Fig. 6),
387 and we have been unable to discern the reasons for this behavior. However, this 958 °C

388 experiment appears anomalous in many ways (see Fig. 4) that may be related to its slightly
389 higher nickel concentration (Table 1).
390
391 The change in the $\ln(\gamma_{Pt}\gamma_{As}^2)$ term inferred from Figure 6 may be attributed to the oxidation of
392 some of the As in the sulfide melt (as discussed above). This oxidation results in an apparently
393 lower activity of As at lower iron concentrations because the oxidized As species are not
394 involved in the sperrylite dissolution reaction (Equation 2a). In addition to the effect of arsenic
395 oxidation on the activity coefficient, the non-ideal mixing between all components in sulfide
396 melts (Kress, 1997; Kress et al., 2008) will also contribute to the changes in the activity
397 coefficient terms.
398
399 Ideally, a quantitative model for sperrylite solubility could be constructed using measurements of
400 all significant intensive variables, but unfortunately we do not have enough data at this time to
401 do so. However, the results of this study combined with those of Helmy et al. (2013a) allow us to
402 constrain the saturation of natural sulfide melts with sperrylite and its mechanisms of formation.
403
404 **Implication for formation of arsenides and sulfarsenides in magmatic sulfide**
405 The results of our study and that of Helmy et al. (2013a) show that As and Pt concentrations
406 necessary for sperrylite saturation in the sulfide melts are much higher than found in natural
407 magmatic sulfide melts. The As concentration in a primitive, high-temperature sulfides with 33
408 wt% sulfur segregating from a mantle-derived basaltic melt is only about 70 ppm (Helmy et al.,
409 2013a), and sulfide droplets in MORB contain 2.8 ppm As (Patten et al., 2013). In natural

410 magmatic Ni-Cu sulfide ores, Pt concentration is typically only at the low parts per million level
411 (Naldrett, 2004), implying that Pt concentrations in an unfractionated sulfide melt at magmatic
412 temperatures are also very low. Our experiments show that sperrylite saturation in a magmatic
413 sulfide melt requires thousands to tens of thousands of ppm of As and Pt at 900-1200 °C. The
414 low As and Pt concentrations in an unfractionated, natural sulfide magmatic melts imply that
415 sperrylite saturation is difficult to reach at magmatic temperatures of 900-1200 °C.
416
417 Our results are not in agreement with the previous arguments that suggested that $PtAs_2$ and other
418 sulfarsenide phases observed in the Platreef of the Bushveld Complex, South Africa (Hutchinson
419 and McDonald, 2008) and in the Creighton Cu-Ni-PGE deposit in Sudbury Igneous Complex,
420 Canada (Dare et al., 2010) formed by crystallization from magmatic sulfide melts at high
421 temperatures.
422
423 Our results indicate that the sulfide melts with low oxygen fugacities and high concentrations of
424 transition metals (particularly iron and nickel) may be the most likely to saturate with sperrylite
425 at low concentrations of As and Pt. A high-iron, low-sulfur melt can lead to a low Pt
426 concentration in the sulfide melt at Pt-metal saturation in an As-free sulfide system (Pruseth and
427 Palme, 2004). At a high iron to sulfur ratio (Fe:S=70:30) the Pt metal solubility only varies from
428 0.03 to 1.1 wt% at 1100-1200 ºC, log fS_2 of -6.03 to -2.6 and log fO_2 of -9.75 to -8.47 (Pruseth
429 and Palme, 2004), much lower than found in our experiments. However, most natural sulfide
430 ores contain less iron and more sulfur (Ebel and Naldrett, 1996), suggesting that the saturation of
431 magmatic sulfide melts with arsenide and sulfarsenide phases is not common in natural sulfide

systems. Although the assimilation of extremely As-rich rocks by an ascending magma might provide the arsenic needed for sperrylite saturation.

Thus, our results imply that saturating sulfide melts with As-bearing PGMs is difficult at temperatures above 900 °C, and most arsenides and sulfarsenides in magmatic sulfide ores probably form by crystallization at low temperatures. Sperrylite crystallization from magmatic sulfide liquids would be restricted to the lower part of magmatic sulfide liquid melting range, where liquids would be Cu-enriched (Craig and Kullerud, 1969).

Acknowledgements This work was supported by a postdoc grant from Canada Research Chair in Magmatic Ore Deposits. Part of this work was performed at Earth & Planetary Sciences, McGill. We also thank for Sadia Medhi and Lang Shi for the help during laser and electron microprobe work. We thank reviewers A. Bell and S. Barnes for their detailed comments which made us question our original interpretations of the data and improve them significantly.

REFERENCES

Bale, C.W., Bélisle, E., Chartrand, P., Decterov, S.A., Eriksson, G., Hack, K., Jung, I-H., Kang, Y-B., Melançon, J., Pelton, A.D., Robelin, C., and Petersen S. (2009) FactSage thermochemical software and databased-recent developments. Calphad, 33, 295–311.

Barin, I. (1995) Thermochemical data of pure substances. VCH Publishers, New York.

Barkov, A.Y., Thibault, Y., Laajoki, K.V.O., Melezhik, V.A., and Nilsson, L.P. (1999) Zoning and substitutions in Co-Ni-(Fe)-PGE sulfarsenides from the Mount General's skaya layered intrusion, arctic Russia. Canadian Mineralogist, 37, 127–142.

455 Barnes, S.-J., and Lightfoot, P.C. (2005) Formation of magmatic nickel-sulfide ore deposits and
456 processes affecting their copper and platinum group element contents. *In* Hedenquist, J.W.,
457 Thompson, J.F.H., Goldfarb, R.J. and Richards, J.P., (eds.), Economic Geology 100th
458 Anniversary Volume, 179–213.
459 Barnes, S.-J., Prichard, H.M., Cox, R.A., Fisher, P.C., and Godel, B. (2008) The location of the
460 chalcophile and siderophile elements in platinum-group element ore deposits (a textural,
461 microbeam and whole rock geochemical study): Implications for the formation of the
462 deposits. Chemical Geology, 248, 295–317.
463 Barnes, S.J., Fisher, L.A., Godel, B., Pearce, M.A., Maier, W.D., Paterson, D., Howard, D.L.,
464 Ryan, C.G., and Laird, J.S. (2016) Primary cumulus platinum minerals in the Monts de
465 Cristal Complex, Gabon: magmatic microenvironments inferred from high-resolution x-ray
466 fluorescence microscopy. Contributions to Mineralogy and Petrology, 171 (23), DOI:
467 10.1007/s00410-016-1232-1.
468 Canali, A.C., and Mungall, J.E. (2015) Solubility of the assemblage Pt-PtAs$_{(melt)}$ in basalt with
469 implications for Pt-As complexing and As speciation. GAC-MAC, Montreal, A34039.
470 Craig, J.R., and Kullerud, G. (1969) Phase relation in the Fe-Ni-Cu-S system and their
471 application to magmatic ore deposits. Economic Geology Monography, 4, 344–358.
472 Dare, S.A.S., Barnes, S.-J., Prichard, H.M., and Fisher, P.C. (2010) The timing and formation of
473 platinum-group minerals from the Creighton Ni-Cu-platinum-group element sulfide deposit,
474 Sudbury, Canada: Early crystallization of PGE-rich sulfarsenides. Economic Geology, 105,
475 1071–1096.

476 Ebel, D.S., and Naldrett, A.J. (1996) Fractional crystallization of sulfide ore liquids at high
477 temperature. Economic Geology, 91, 607–621.
478 Farrow, C.E.G., and Watkinson, D.H. (1997) Diversity of precious-metal mineralization in
479 footwall Cu-Ni-PGE deposits, Sudbury, Ontario: Implications for hydrothermal models of
480 formation. Canadian Mineralogist, 38, 817–839.
481 Fleet, M.E., Chryssoulis, S.L., Stone, W.E., and Weisener, G. (1993) Partitioning of platinum-
482 group elements and Au in the Fe-Ni-Cu-S system: Experiments on the fractional
483 crystallization of sulfide melts. Contributions to Mineralogy and Petrology, 115, 36–44.
484 Fonseca, R.O.C., Campbell, I.H., O'Neill, H.S.C., and Allen, C.M. (2009) Solubility of Pt in
485 sulphide mattes: Implications for the genesis of PGE-rich horizons in layered intrusions.
486 Geochimica et Cosmochimica Acta, 73, 5764–5777.
487 Gervilla, F., Papunen, H., Kojonen, K., and Johanson, B. (1998) Platinum-, palladium- and gold-
488 rich arsenide ores from the Kylmäkoski Ni-Cu deposit (Vammala nickel belt, SW Finland).
489 Mineralogy and Petrology, 64, 163–185.
490 Godel, B., González-Álvarez, I., Barnes, S.J., Barnes, S.-J., Parker, P., and Day, J. (2012)
491 Sulfides and sulfarsenides from the Rosie nickel Prospect, Duketon Greenstone Belt,
492 Western Australia. Economic Geology, 107, 275–294.
493 Hanley, J.J. (2007) The role of arsenic-rich melts and mineral phases in the development of high-
494 grade Pt-Pd mineralization within komatiite-associated magmatic Ni-Cu sulfide horizons at
495 Dundonald Beach South, Abitibi subprovince, Ontario, Canada. Economic Geology, 102,
496 305–317.

497 Helmy, H.M., Ballhaus, C., Wohlgemuth-Ueberwasser, C., Fonseca, R.C., and Laurenz, V.
498 (2010) Partitioning of Se, As, Sb, Te and Bi between monosulfide solid solution and sulfide
499 melt-Application to magmatic sulfide deposits. Geochimica et Cosmochimica Acta, 74,
500 6174–6179.
501 Helmy, H.M., Ballhaus, C., Fonseca, R.O.C., and Nagel, T.J (2013a) Fractionation of platinum,
502 palladium, nickel, and copper in sulfide-arsenide systems at magmatic temperature.
503 Contributions to Mineralogy and Petrology, 166, 1725–1737.
504 Helmy, H.M., Ballhaus, C., Fonseca, R.O.C., Wirth, R., Nagel, T.J., and Tredoux, M. (2013b)
505 Noble metal nanoclusters and nanoparticles precede mineral formation in magmatic sulphide
506 melts. Nature, doi:10.1038/ncomms3405.
507 Holwell, D.A., and McDonald, I. (2006) Petrology, geochemistry and the mechanisms
508 determining the distribution of platinum-group element and base metal sulphide
509 mineralization in the Platreef at Overysel, northern Bushveld Complex, South Africa.
510 Mineralium Deposita, 41, 575–598.
511 Holwell, D.A., and McDonald, I. (2007) Distribution of platinum-group elements in the Platreef
512 at Overysel, northern Bushveld Complex: A combined PGM and LA-ICP-MS study.
513 Contributions to Mineralogy and Petrology, 154, 171–190.
514 Holwell, D.A., and McDonald, I. (2010) A review of the behavior of platinum group elements
515 within natural magmatic sulfide ore systems. Platinum Metals Review, 54, 26–36.
516 Hutchinson, D., and McDonald, I. (2008) Laser ablation ICP-MS study of platinum-group
517 elements in sulphides from the Platreef at Turfspruit, northern limb of the Bushveld
518 Complex, South Africa. Mineralium Deposita, 43, 695–711.

519 Kress, V. (1997) Thermochemistry of sulfide liquids. I. The system O-S-Fe at 1 bar.
520 Contributions to Mineralogy and Petrology, 127, 176–186.
521 Kress, V., Greene, L.E., Ortiz, M.D., and Mioduszewski, K. (2008) Thermochemistry of sulfide
522 liquids IV: density measurements and the thermodynamics of O-S-Fe-Ni-Cu liquids at low to
523 moderate pressures. Contributions to Mineralogy and Petrology, 156, 785–797.
524 Li, C., Ripley, E.M., Oberthür, T., Miller, J.D., and Joslin, G.D. (2008) Textural, mineralogical
525 and stable isotope studies of hydrothermal alteration in the main sulfide zone of the Great
526 Dyke, Zimbabwe and the precious metals zone of the Sonju Laker Intrusion, Minnesota,
527 USA. Mineralium Deposita, 44, 97–110.
528 Liu, Y., and Brenan, J. (2015) Partitioning of platinum-group elements (PGE) and chalcogens
529 (Se, Te, As, Sb, Bi) between monosulfide solid solution (MSS), intermediate solid solution
530 (ISS) and sulfide liquid at controlled fO_2-fS_2 conditions. Geochimica et Cosmochimica Acta,
531 159, 139–161.
532 Maier, W., Rasmussen, B., Fletcher, I., Godel, B., Barnes, S.J., Fisher, L., and Yang, S. (2015)
533 Petrogenesis of the ~2.77 Ga Monts de Cristal complex, Gabon: Evidence for direct
534 precipitation of Pt-arsenides from basaltic magma. Journal of Petrology, 56, 1285–1308.
535 Mungall, J.E., Andrews, D.R.A., Cabri, L.J., Sylvester, P. J., and Tubrett, M. (2005) Partitioning
536 of Cu, Ni, Au, and platinum-group elements between monosulfide solid solution and sulfide
537 melt under controlled oxygen and sulfur fugacities. Geochimica et Cosmochimica Acta, 69,
538 4349–4360.

539 Mungall, J.E., and Su, S. (2005) Interfacial tension between magmatic sulfide and silicate
540 liquids: Constrains on kinetics of sulfide liquation and sulfide migration through silicate
541 rocks. Earth and Planet Science Letter, 234, 135–149.
542 Naldrett, A.J. (1969) A portion of the system Fe-O-S between 900 and 1080 °C and its
543 application to sulfide ore magmas. Journal of Petrology, 10, 171–201.
544 Naldrett, A.J. (2004) Magmatic sulfide deposits: Geology, Geochemistry and Exploration.
545 Springer, New York, pp. 1–20.
546 Pattern, C., Barnes, S.-J., Mathez, E.A., and Jenner, F.E. (2013) Partition coefficient of
547 chalcophile elements between sulfide and silicate melts and the early crystallization history
548 of sulfide liquid: LA-ICP-MS analysis of MORB sulfide droplet. Chemical Geology, 358,
549 170–188.
550 Piña, R., Gervilla, F., Barnes, S.-J., Ortega, L., and Lunar, R. (2012a) Distribution of platinum-
551 group and chalcophile elements in the Aguablanca Ni-Cu sulfide deposit (SW Spain):
552 Evidence from a LA-ICP-MS study. Chemical Geology, 302–303, 61–75.
553 Piña, R., Gervilla, F., Barnes, S.-J., Ortega, L., and Lunar, R. (2012b) Partition of platinum-
554 group elements between arsenide and sulfide minerals in magmatic Ni-Cu sulfide systems.
555 12th international Ni-Cu-(PGE) Symposium, Guiyang, China.
556 Piña, R., Gervilla, F., Barnes, S.-J., Ortega, L., and Lunar, R. (2013) Platinum-group elements-
557 bearing pyrite from the Aguablanca Ni-Cu sulphide deposit (SW Spain): a LA-ICP-MS
558 study. European Journal of Mineralogy, 25, 241–252.
559 Prichard, H. M., Fisher, P. C., MCdonald, I., Knight, R. D., Sharp, D. R., and Williams, J. P.
560 (2013) The distribution of PGE and the role of arsenic as a collector of PGE in the Spotted

Quoll nickel ore deposit in the Forrestania Greenstone Belt, Western Australia. Economic Geology, 108, 1903–1921.

Pruseth, K.L., and Palme, H. (2004) The solubility of Pt in liquid Fe-sulfides. Chemical Geology, 208, 233–245.

Rasband, W.S. (2005) ImageJ, U.S. National Institutes of Health, Bethesda, Maryland, USA. http://rsb.info.nih.gov/ij/.

Sinyakova, E.F., and Kosyakov, V.I. (2012) The behavior of noble-metal admixtures during fractional crystallization of As- and Co-containing Cu-Fe-Ni sulfide melts. Russia Geology and Geophysics, 53, 1055–1076.

Tomkins, A.G. (2010) Wetting facilitates late-stage segregation of precious metal-enriched sulfosalt melt in magmatic sulfide systems. Geology, 38, 951–954.

583 **FIGURE CAPTIONS**

584 **Fig. 1**. Experimental capsule for this sperrylite saturation study.

585

586 **Fig. 2**. BSE images of sectioned run products. **a.** Experiment SPT5 shows the equilibrium *mss*
587 coexists with the sulfide melt. The bright phases in the melt regions are quenched base metal
588 sulfide liquid (BMS-l) rich in As and Pt, which occur within quenched *iss* (q-*iss*) as quenched
589 $PtAs_2$ crystals or As droplets. **b.** Quenched sulfide melt from experiment SPT15 consists of
590 quenched *mss* (q-*mss*), q-*iss*, quenched BMS-l, lamellae to dendritic quench $PtAs_2$ crystals
591 (bright phases distributed within quenched BMS-l or at the boundary of q-*mss*), and As droplet
592 rich in As and Pt. **c.** Larger quench $PtAs_2$ crystals in the sulfide melt from experiment SPT9
593 quenched at 910 °C. **d.** A sub-spherical As droplet within the sulfide melt from SPT20 quenched
594 at 1000 °C. Note the irregular to dendritic grey-white crystals exsolved within the As droplet.
595 The dark-grey matrix of the droplet is rich in As. **BMS-l**, quenched base metal sulfide liquid rich
596 in As and Pt; **As-dpt**, As droplet.

597

598 **Fig. 3**. Major element compositions in melts of differing duration from low-temperature
599 experiments at 930 °C. The compositions of Fe, S, Ni, and Cu in experiments of 12.4 and 24 h
600 demonstrate that steady state behavior, if not equilibrium, is rapidly established in the
601 experiments.

602

603 **Fig. 4**. **a.** The relation between As concentration in the sulfide melt at sperrylite saturation and
604 the iron concentration of the melt. Each data point in all panels of this figure includes the 1-

sigma uncertainties based upon multiple analyses and is accompanied by the temperature of the experiment (see Table 1). Also shown in each panel are the results of Helmy et al.'s (2013a) study of sperrylite saturation in nickel-rich Fe-Ni-Cu-S melts. Note that our experiments at the same, or similar temperatures display a linear relationship with a negative slope. **b.** The relation between Pt concentration in the sulfide melt at sperrylite saturation and the iron concentration of the melt, which also display linear relationships with negative slopes as seen in 4a. **c.** The relation between As concentration in sperrylite-saturated equilibrium *mss* and its iron concentration. There is a weak correlation between the iron concentration and the As concentration, but no clear relation with temperature is seen. **d.** The relation between Pt concentration in sperrylite-saturated equilibrium *mss* and its iron concentration, which behaves similarly to As in 4c.

Fig. 5. Concentration of As versus Pt in sperrylite-saturated melts at 980 to 1060 °C from this study and from Helmy et al. (2013a). The concentrations of As and Pt are expressed in moles/100 g of solution. The concentrations in As and Pt in *mss*-undersaturated melts define a line with a slope of 2.1, consistent with a dissolution reaction of $PtAs_2^{sperrylite} \Leftrightarrow Pt^{melt} + 2\ As^{melt}$ (see discussion of equation 2a). However, *mss*-saturated melts are depleted in Pt when compared to the line due to Pt incorporation into equilibrium *mss*.

Fig. 6. van't Hoff plot of the solubility product of $X_{Pt}X_{As}^2$ versus 10 000/T in sperrylite-saturated melts of this study with the $X_{Fe}/(X_{Fe}+X_S)_{melt}$ of each melt noted. The data with low $X_{Fe}/(X_{Fe}+X_S)_{melt}$ between 0.356 and 0.370 were fit to extract an enthalpy of reaction from the

627 slope. The constancy of ΔH (slope) was then tested by using it to fit the two data points with high
628 $X_{Fe}/(X_{Fe}+X_S)_{melt}$, 0.458 and 0.466 and the figure contoured with different intercepts that can be
629 equated with the sum of $\Delta S/R + \ln(\gamma_{Pt}\gamma_{As}^2)$ in the van't Hoff equation. Assuming constant ΔS, the
630 change in intercepts required by the results reflects changes in the activity coefficient term due to
631 varying iron concentrations in the melts. See text for a full discussion.
632
633 **Table 1**. Experimental conditions and compositions of quenched sulfide melts and equilibrium
634 *mss* from LA-ICP-MS analysis.
635
636 **Table 2**. Compositions of each phase in quenched sulfide melts from microprobe analysis (wt%).

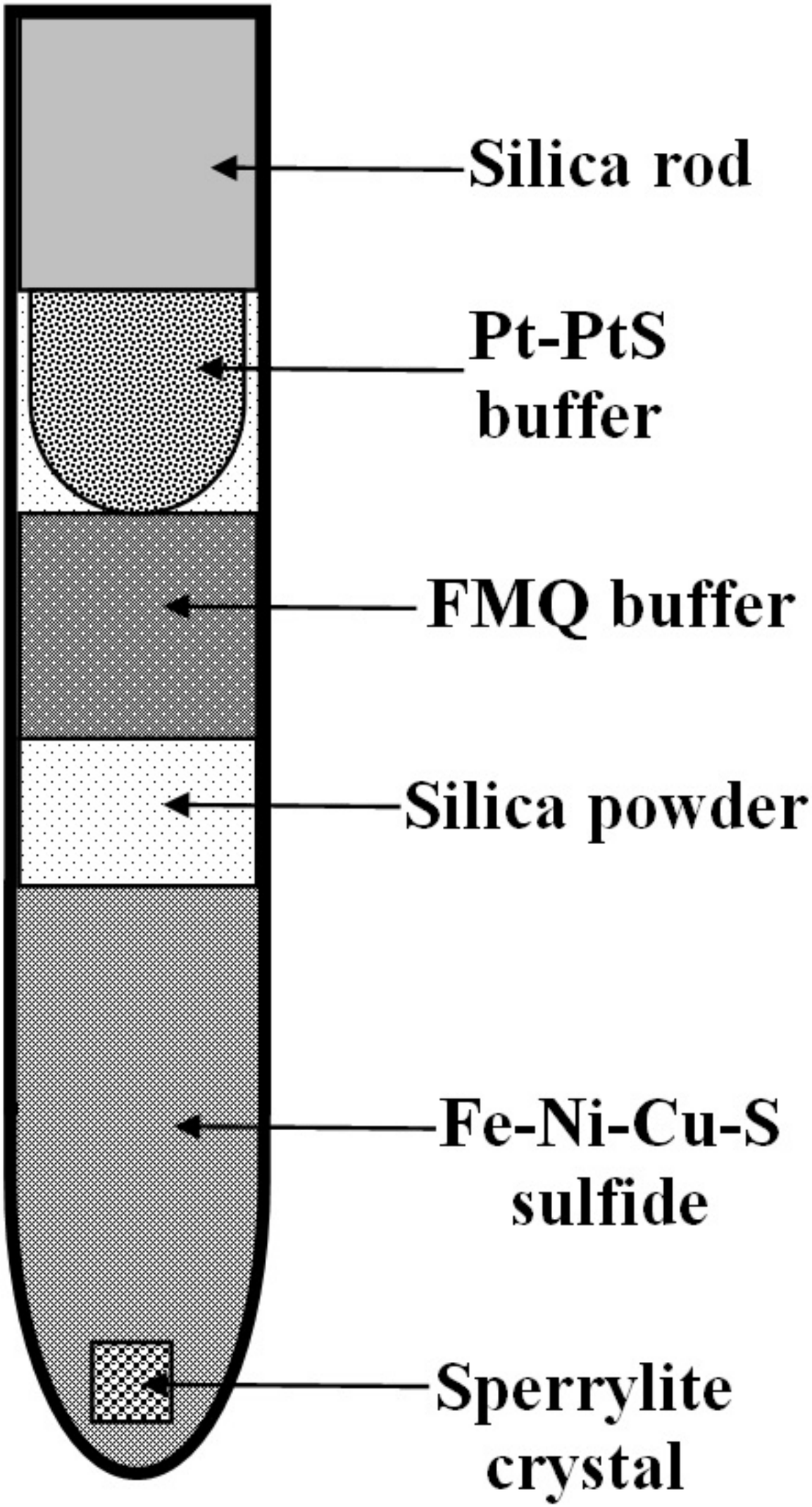
Silica rod
Pt-PtS
buffer
FMQ buffer
Silica powder
Fe-Ni-Cu-S
sulfide
Sperrylite
crystal

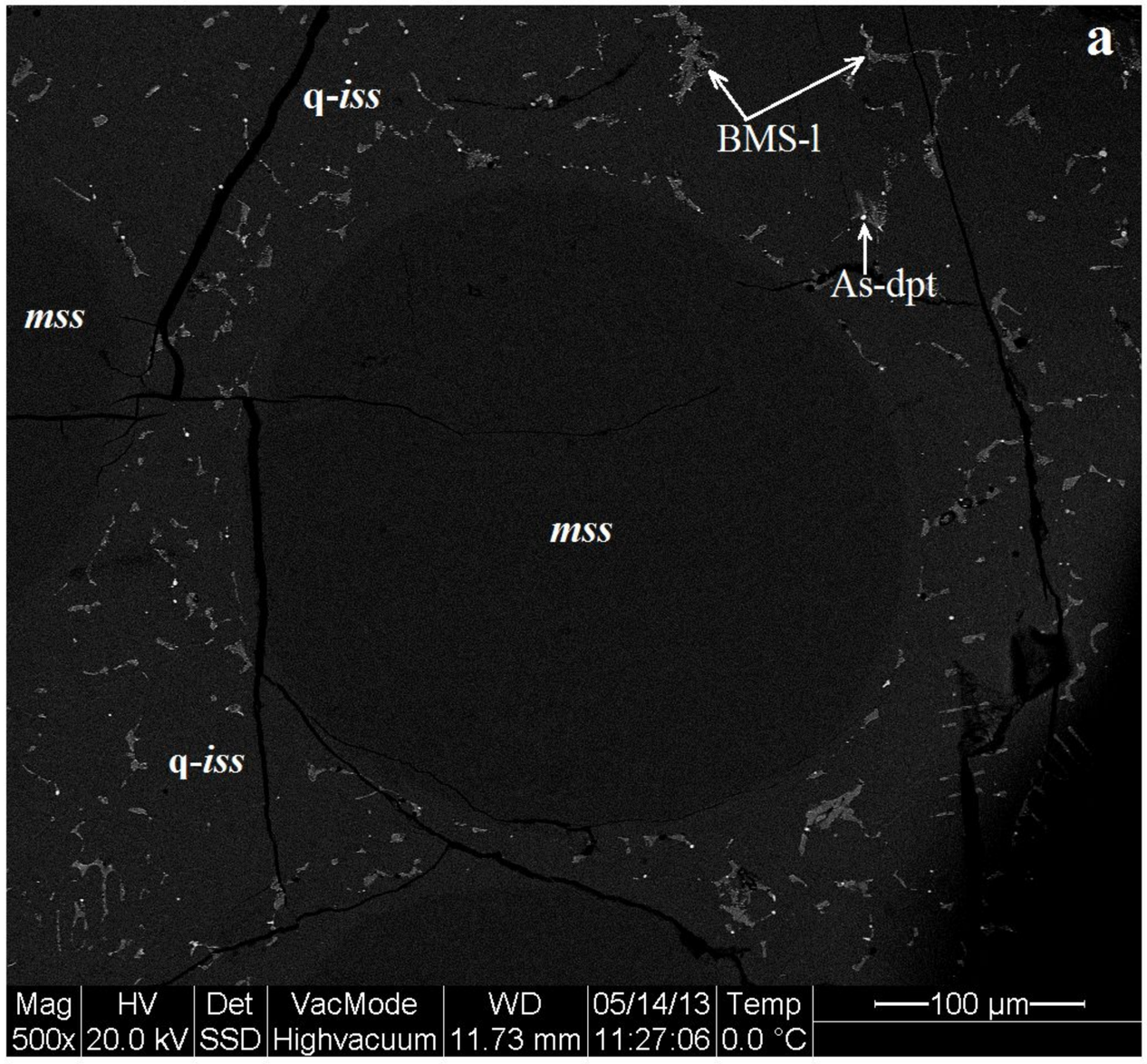
a
q-*iss*
BMS-l
As-dpt
mss
mss
q-*iss*
Mag 500x
HV 20.0 kV
Det SSD
VacMode Highvacuum
WD 11.73 mm
05/14/13 11:27:06
Temp 0.0 °C
100 µm

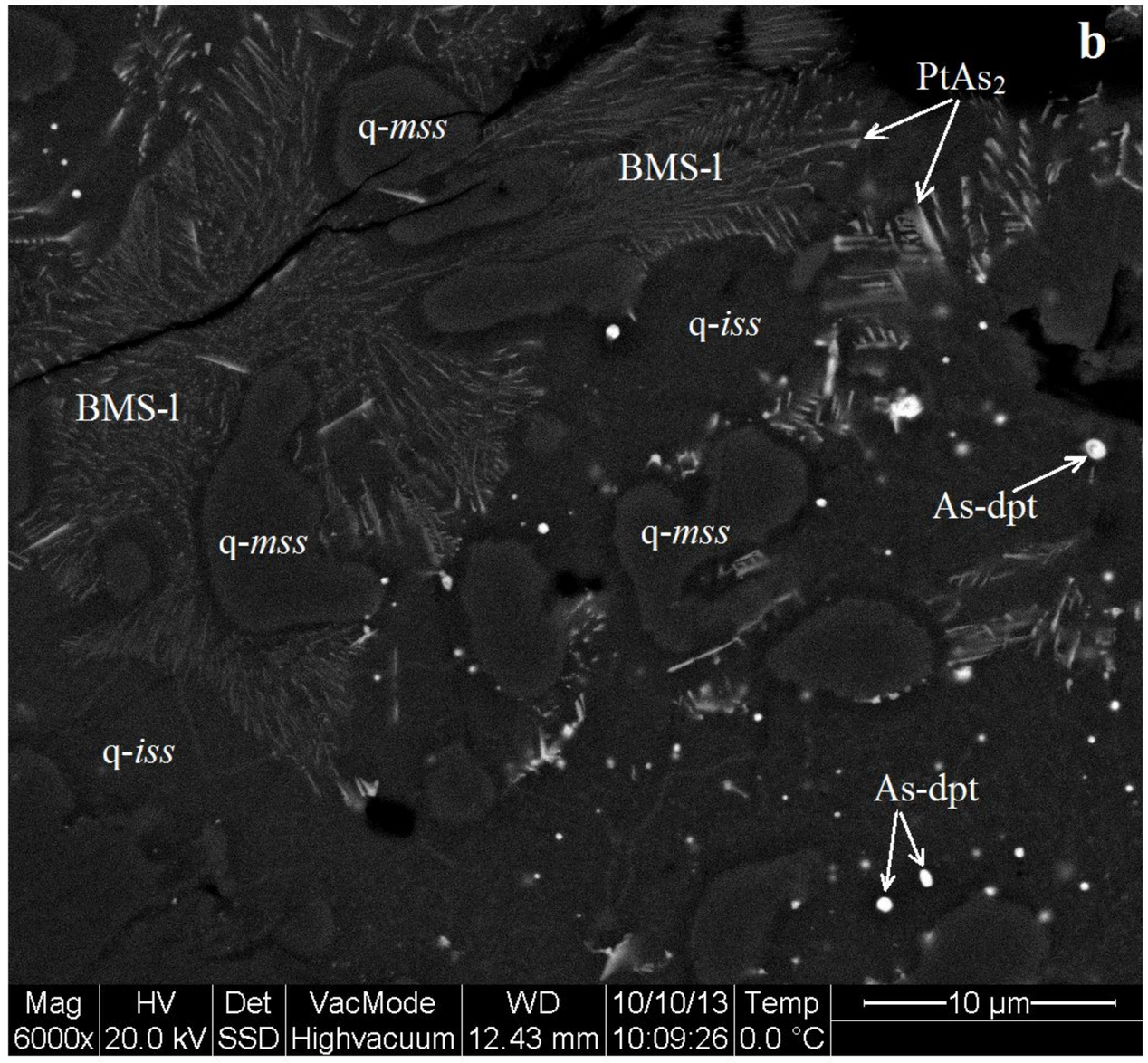
b
PtAs$_2$
q-*mss*
BMS-l
q-*iss*
BMS-l
As-dpt
q-*mss*
q-*mss*
q-*iss*
As-dpt
Mag 6000x
HV 20.0 kV
Det SSD
VacMode Highvacuum
WD 12.43 mm
10/10/13 10:09:26
Temp 0.0 °C
10 µm

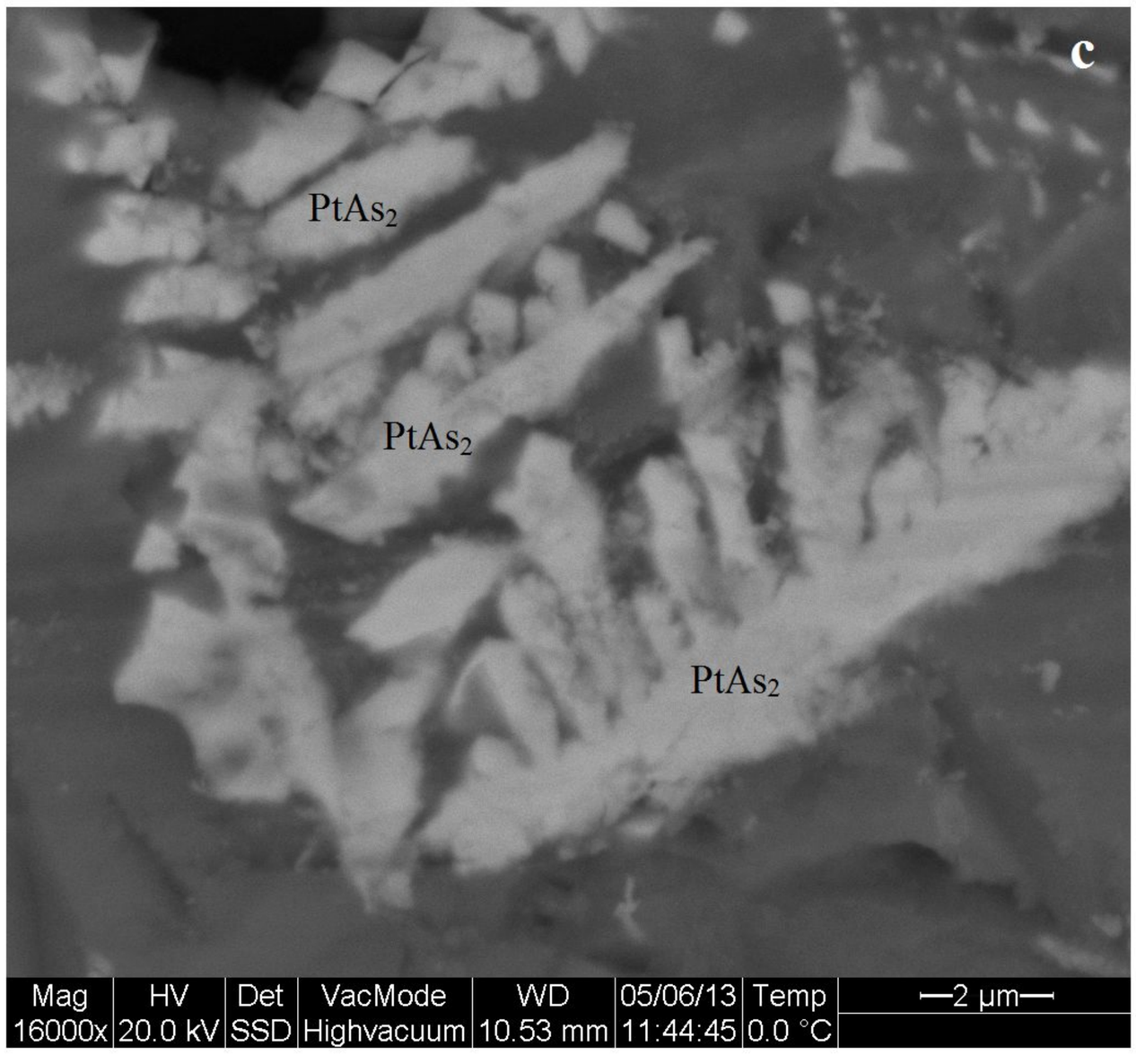
c
PtAs$_2$
PtAs$_2$
PtAs$_2$
Mag 16000x
HV 20.0 kV
Det SSD
VacMode Highvacuum
WD 10.53 mm
05/06/13 11:44:45
Temp 0.0 °C
2 µm

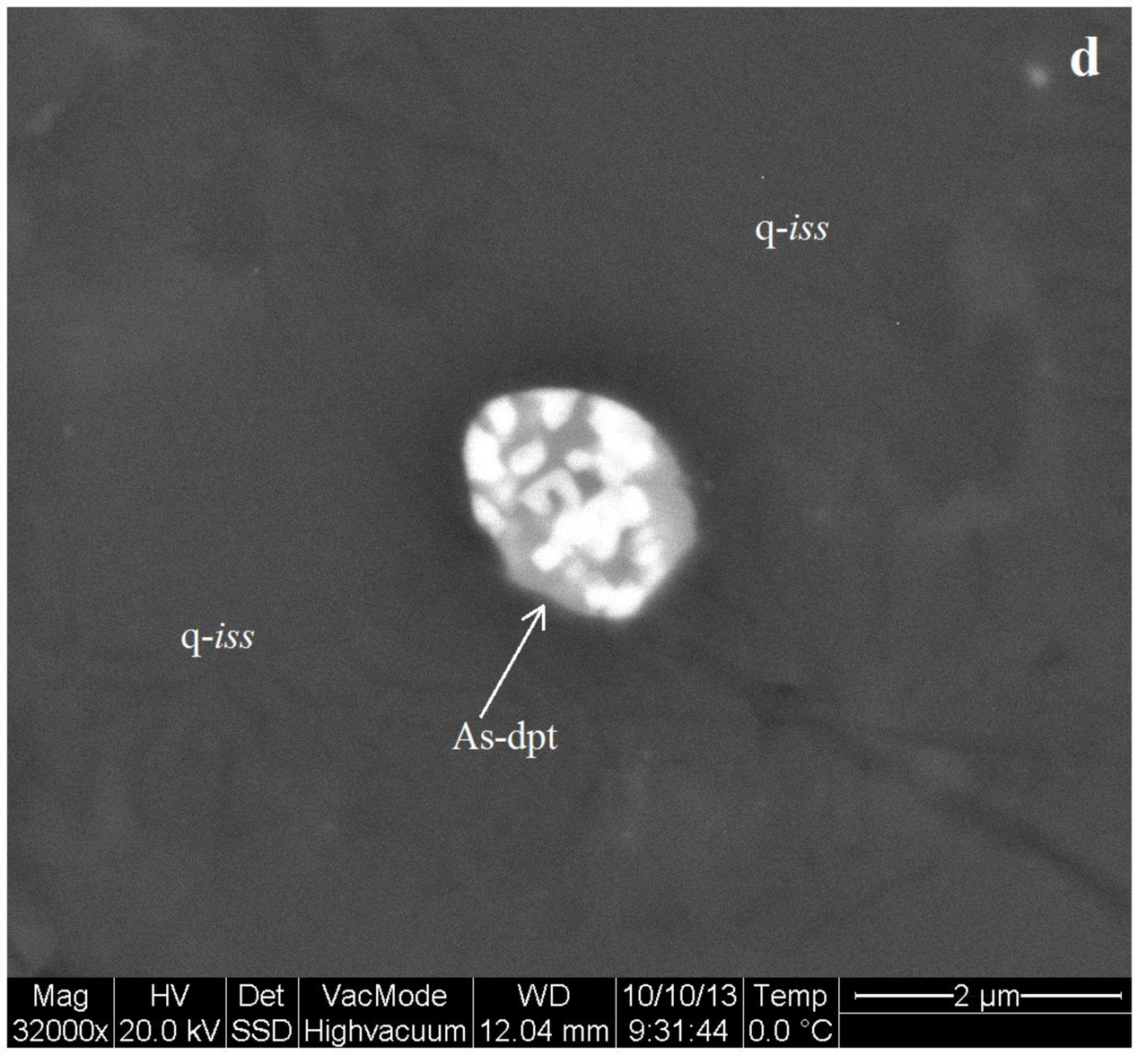
d
q-*iss*
q-*iss*
As-dpt
Mag 32000x
HV 20.0 kV
Det SSD
VacMode Highvacuum
WD 12.04 mm
10/10/13 9:31:44
Temp 0.0 °C
2 µm

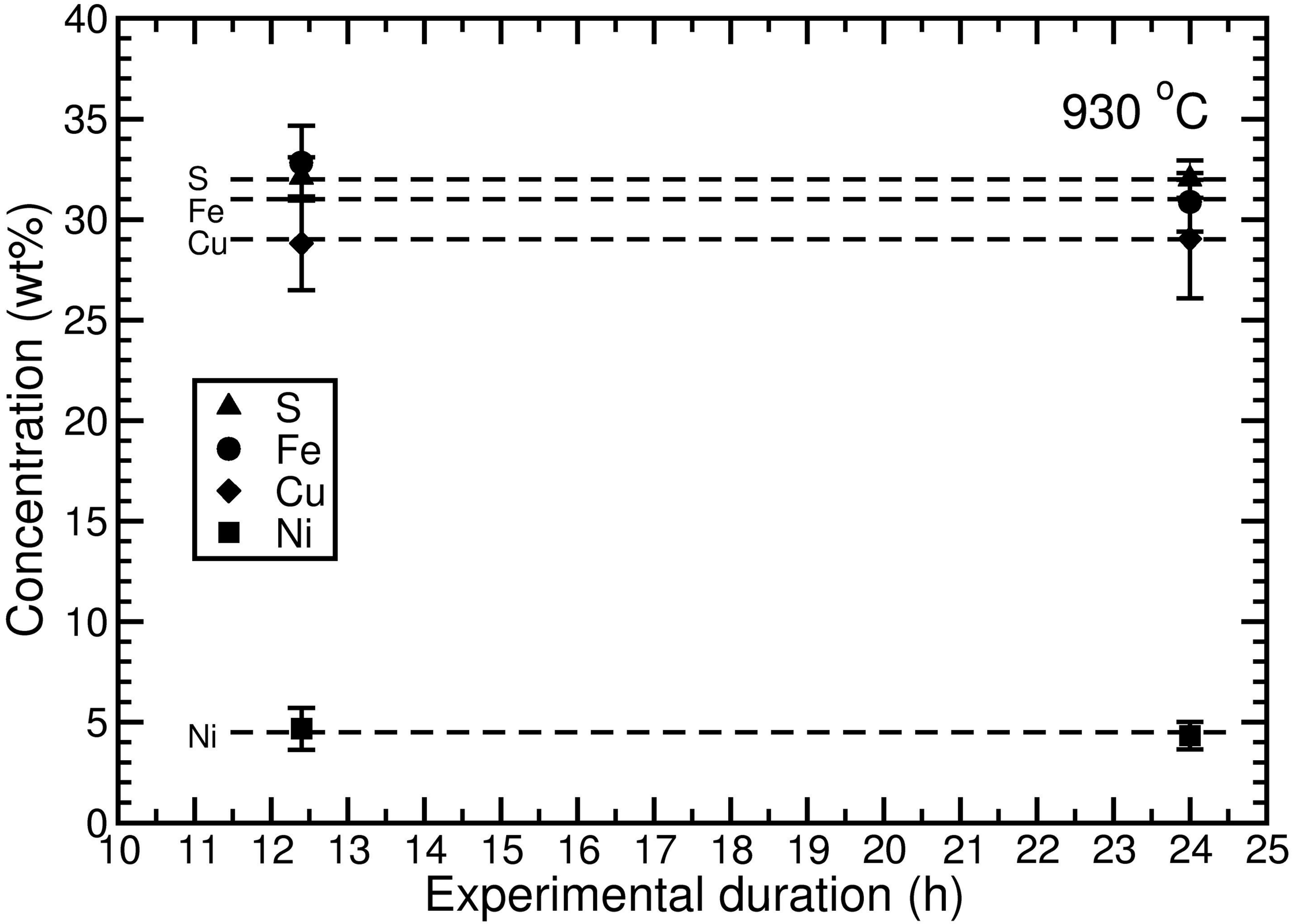
930 °C
S
Fe
Cu
Ni
Concentration (wt%)
Experimental duration (h)
0
5
10
15
20
25
30
35
40
10
11
12
13
14
15
16
17
18
19
20
21
22
23
24
25

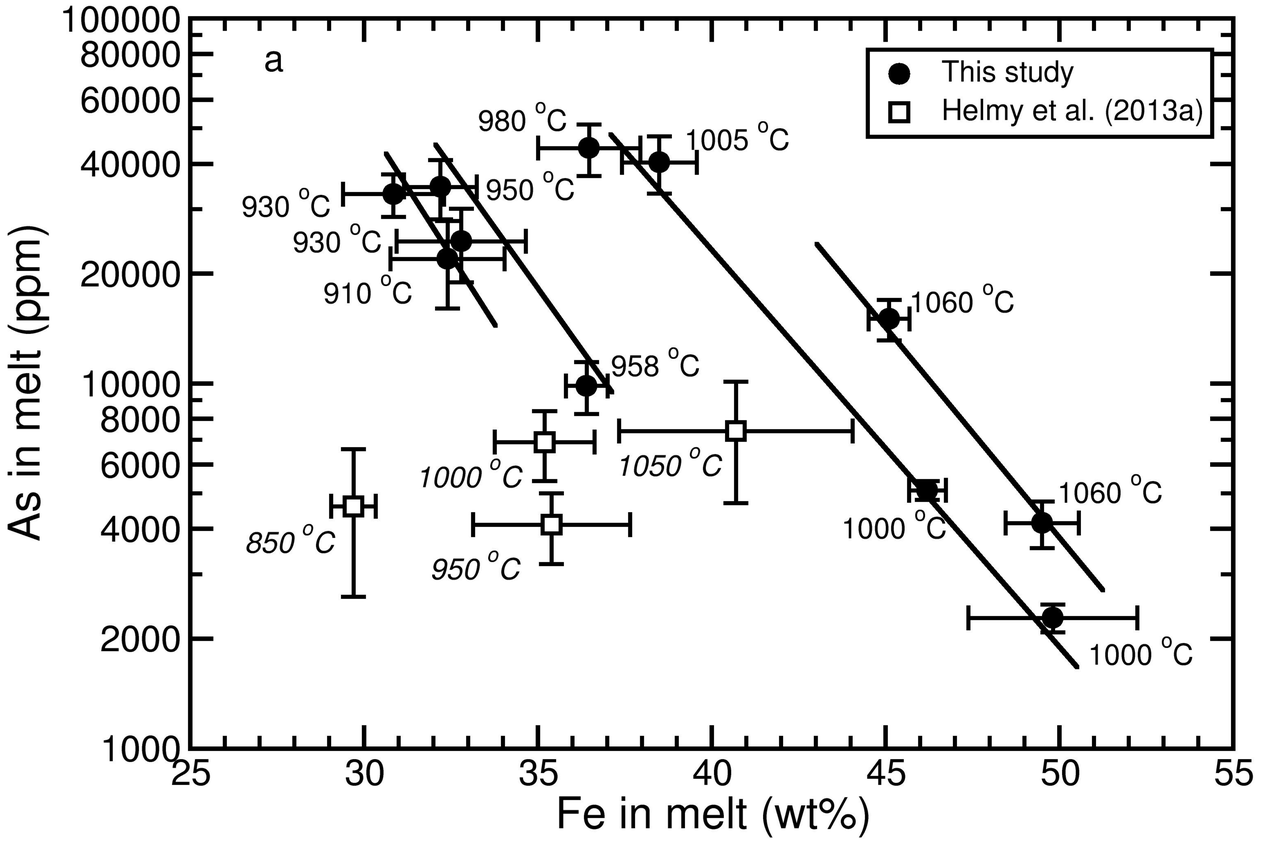
a
This study
Helmy et al. (2013a)
980 °C
1005 °C
950 °C
930 °C
930 °C
910 °C
1060 °C
958 °C
1000 °C
1050 °C
1060 °C
850 °C
950 °C
1000 °C
As in melt (ppm)
Fe in melt (wt%)

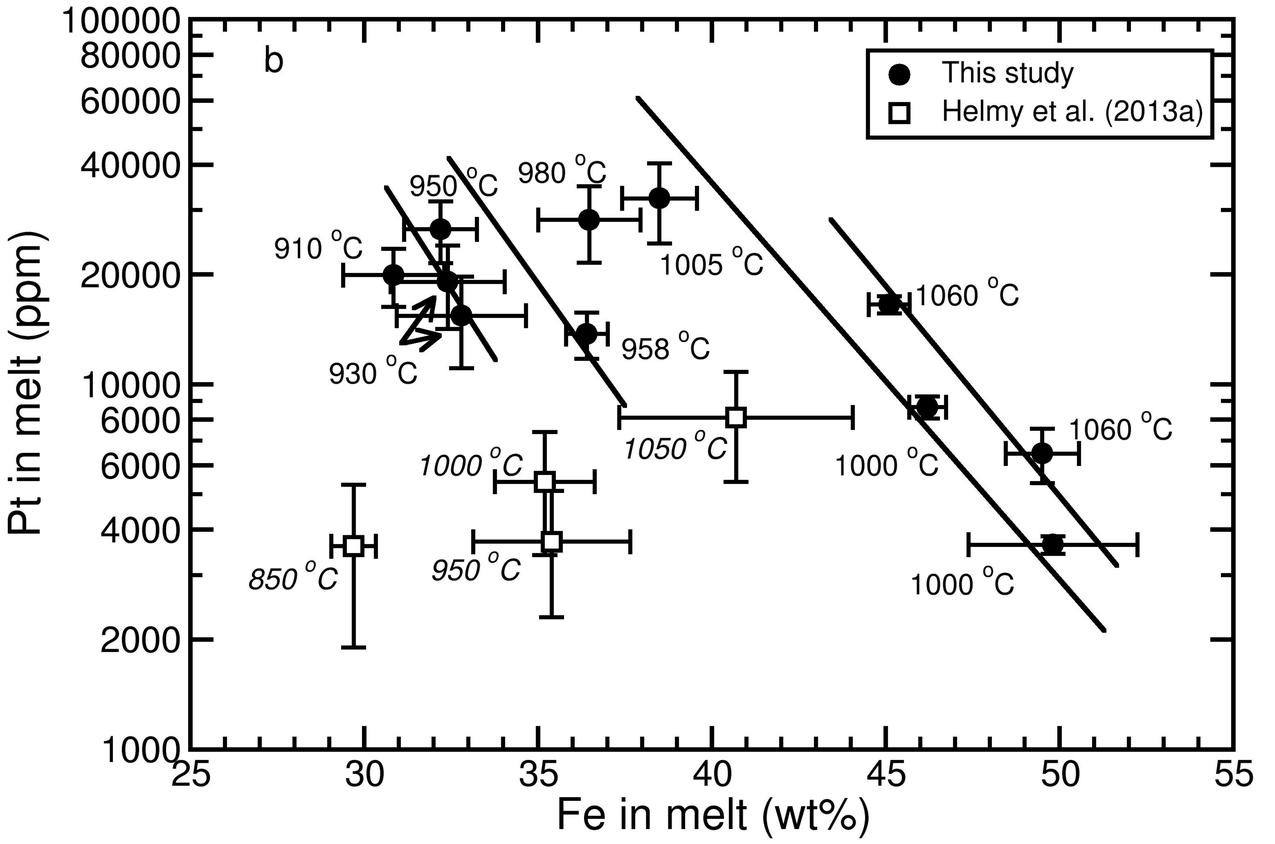
b
This study
Helmy et al. (2013a)
950 °C
980 °C
910 °C
1005 °C
930 °C
958 °C
1060 °C
1050 °C
1000 °C
1060 °C
1000 °C
850 °C
950 °C
Pt in melt (ppm)
Fe in melt (wt%)

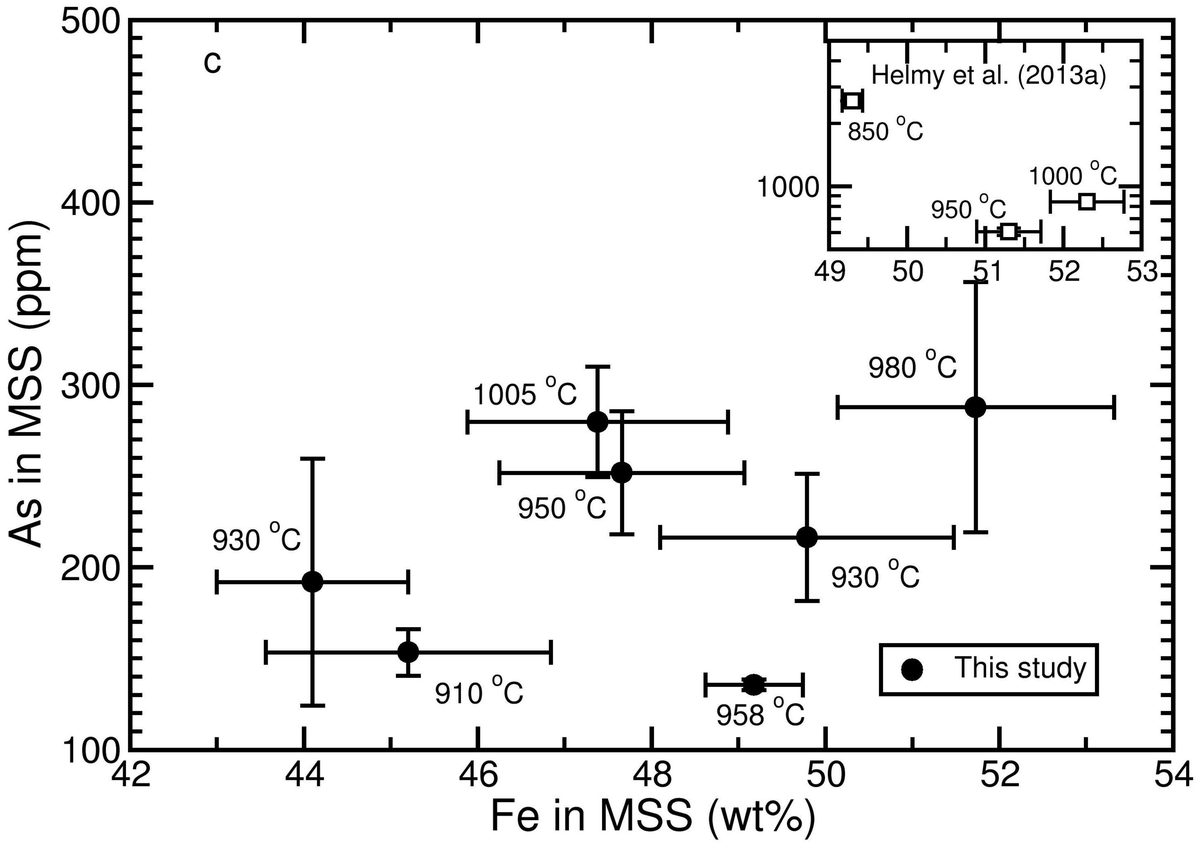
c
Helmy et al. (2013a)
850 °C
1000 °C
950 °C
980 °C
1005 °C
950 °C
930 °C
930 °C
910 °C
958 °C
This study
As in MSS (ppm)
Fe in MSS (wt%)

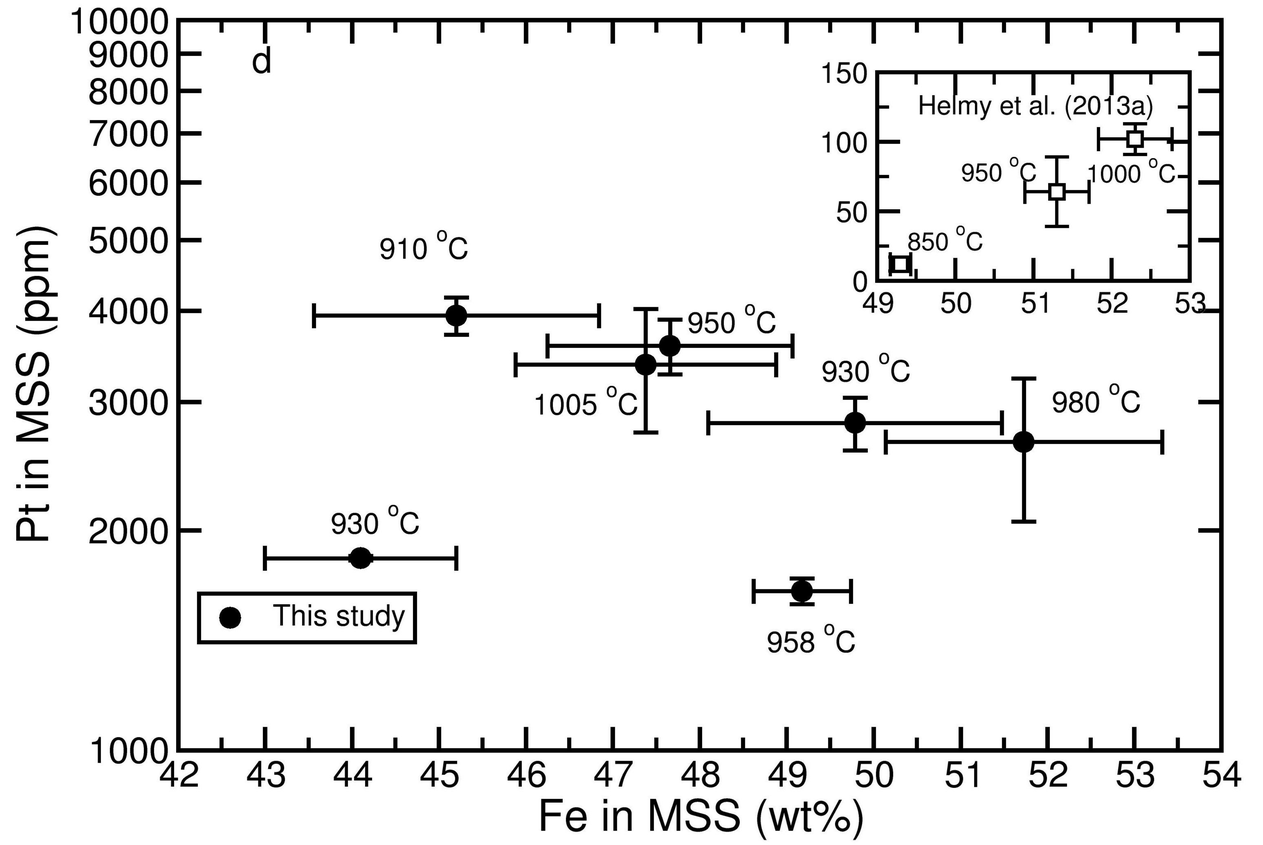
d
Helmy et al. (2013a)
950 °C
1000 °C
850 °C
910 °C
950 °C
1005 °C
930 °C
980 °C
930 °C
This study
958 °C
Pt in MSS (ppm)
Fe in MSS (wt%)

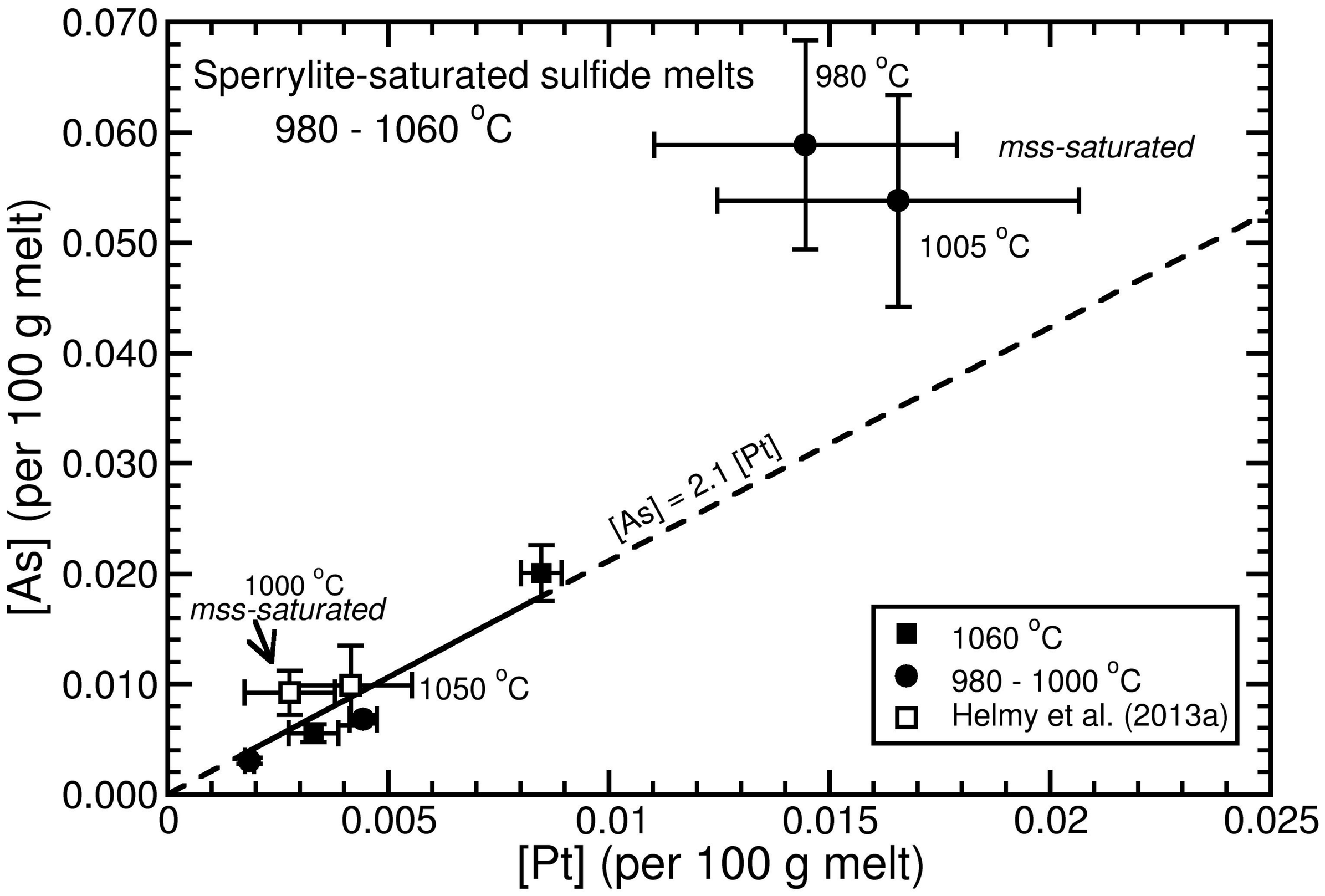
Sperrylite-saturated sulfide melts
980 - 1060 °C
980 °C
mss-saturated
1005 °C
[As] = 2.1 [Pt]
1000 °C
mss-saturated
1050 °C
1060 °C
980 - 1000 °C
Helmy et al. (2013a)
[As] (per 100 g melt)
[Pt] (per 100 g melt)
0.070
0.060
0.050
0.040
0.030
0.020
0.010
0.000
0
0.005
0.01
0.015
0.02
0.025

$$\ln (X_{Pt} X_{As}^2) = -\Delta H^o/R\ (1/T) + \Delta S^o/R - \ln(\gamma_{Pt}\ \gamma_{As}^2)$$

$PtAs_2$ sperrylite $\leftrightarrow$ Pt + 2 As

$\ln(X_{Pt} X_{As}^2) = (-45\,082 +/- 24\,070/T) + 24.0 +/- 20.0$

$\ln (X_{Pt} X_{As}^2)_{melt}$ at sperrylite saturation

$\left(\frac{Fe}{Fe+S}\right)_{molar}$

0.406
0.405
0.358
0.356
0.370
0.367
0.434
0.397
0.441
0.458
0.466

intercept = 22
intercept = 20
intercept = 18
intercept = 16
intercept = 14

-10.0
-12.0
-14.0
-16.0
-18.0
-20.0
-22.0

7.4
7.6
7.8
8
8.2
8.4
8.6

10000/T(K)

Table 1 Experimental conditions and compositions of quenched sulfide melts and equilibrium *mss* from LA-ICP-MS analysis.

Sample	T (°C)	fO_2 (log) (bars)	fS_2 (log) (bars)	Run time (h)	Compositions of initial Fe-Ni-Cu-S mixture (wt%)					Compositions of quenched sulfide melts and equilibrium *mss* (wt%)[a]									$PtAs_2$ solubility in melt and equilibrium *mss* (ppm)	
					Fe	Ni	Cu	S	Atomic Metal/S	Fe	Ni	Cu	S	As[b]	Pt[b]	Total	Atomic Metal/S	Atomic As/Pt		
SPT20	1000	-12.02	-2.74	46.5	48.88	7.02	8.11	35.99	1.0	49.82±2.43	6.67±0.09	9.84±1.62	32.83±0.49	0.2276±0.02	0.3628±0.02	99.75	1.14	1.63	5620.7	**melt**
SPT17	1060	-11.10	-2.21	43	48.88	7.02	8.11	35.99	1.0	49.51±1.05	6.6±0.13	8.8±1.52	33.67±0.15	0.414±0.06	0.645±0.11	99.64	1.09	1.67	10159.3	**melt**
SPT15	958	-12.71	-3.13	57	46.09	7.26	9.66	36.98	0.95	36.41±0.67	8.04±0.24	21.04±0.99	31.77±0.38	0.9835±0.16	1.372±0.20	99.62	1.14	1.87	23266.5	**melt**
										49.18±0.56	7.34±0.26	4.88±0.15	38.34±0.77	135.5±2.99	1650.2±67	99.92	0.91	0.22	658.5	***mss***
SPT21	1000	-12.02	-2.74	46.5	46.97	7.18	8.58	37.01	0.95	46.21±0.53	7.28±0.11	11.1±0.73	33.6±0.27	0.5092±0.03	0.865±0.06	99.56	1.08	1.53	12876.7	**melt**
SPT16	1060	-11.10	-2.21	43	46.09	7.26	9.66	36.98	0.95	45.11±0.59	7.52±0.15	9.93±0.53	33.75±0.24	1.502±0.19	1.653±0.09	99.47	1.05	2.37	32830.0	**melt**
SPT5[c]	910	-13.56	-3.59	167.3	43.77	7.31	10.98	37.94	0.91	31.72±0.39	4.35±0.18	30.6±0.85	31.54±0.41	0.0261±0.01	0.874±0.28	99.11	1.15			**melt**
										50.88±0.82	7.18±0.21	6.87±0.47	36.76±0.56	15.44±0.66	1129.6±45	101.8	1.00			***mss***
SPT12	930	-13.20	-3.40	12.4	43.93	8.8	9.17	38.1	0.91	32.8±1.86	4.67±1.04	28.8±2.33	32.1±0.98	2.45±0.56	1.54±0.433	102.36	1.13	4.14	43041.1	**melt**
										44.1±1.1	9.61±0.61	6.73±0.38	37.82±1.15	191.8±67.7	1831.3±13	98.46	0.90	0.27	872.2	***mss***
SPT3	1000	-12.02	-2.74	186	43.77	7.31	10.98	37.94	0.91	41.5±0.65	6.7±0.24	18.5±1.85	33±0.49	0.8773±0.14	1.15±0.15	101.73	1.12			**melt**
										49.7±0.79	7.26±0.30	4.37±0.17	38.5±0.51	81.6±2.5	1064.7±51	99.94	0.90			***mss***
SPT14	1005	-11.94	-2.69	24	43.93	8.8	9.17	38.1	0.91	38.5±1.08	6.77±0.95	17.5±2.14	32.4±1.47	4.03±0.72	3.23±0.80	102.43	1.09	3.25	76572.9	**melt**
										47.38±1.5	9.33±0.48	4.5±0.46	38±1.04	279.6±30.2	3370.8±647	99.58	0.91	0.22	1360.5	***mss***
SPT9	910	-13.56	-3.59	30	40.89	7.66	8.26	43.18	0.74	32.41±1.64	3.51±0.50	29.08±2.75	32.03±1.01	2.192±0.59	1.907±0.49	101.13	1.11	2.99	43487.4	**melt**
										45.2±1.04	9.27±0.49	7.46±0.27	38.3±1.57	153.3±12.8	3936±231.4	100.64	0.91	0.10	950.3	***mss***
SPT10	930	-13.20	-3.40	24	40.89	7.66	8.26	43.18	0.74	30.85±1.45	4.32±0.68	29.02±2.95	32±0.93	3.299±0.44	1.9901±0.36	101.48	1.10	4.32	57574.7	**melt**
										49.79±1.69	8.55±0.41	6.78±0.47	36.94±2.11	216.3±34.9	2805±233.6	102.36	0.99	0.20	1048.6	***mss***
SPT11	950	-12.85	-3.20	12	40.89	7.66	8.26	43.18	0.74	32.2±1.05	5.23±0.57	23.61±2.11	33.1±1.42	3.453±0.64	2.657±0.51	100.25	1.02	3.38	66169.4	**melt**
										47.66±1.41	8.91±0.32	5.65±0.26	36.76±2.17	251.7±33.7	3578±307.4	99.36	0.96	0.18	1297.0	***mss***
SPT13	980	-12.34	-2.92	14	40.89	7.66	8.26	43.18	0.74	36.48±1.47	5.61±0.94	21.19±2.46	30.8±0.72	4.41±0.71	2.82±0.67	101.31	1.14	4.07	78456.5	**melt**
										51.73±1.59	8.39±0.36	5.05±0.39	35.96±1.24	287.6±68.6	2642±586	101.42	1.03	0.28	1254.0	***mss***

a: The standard derivation was calculated from results of total 3-22 analyzed laser lines for each sample.

b: The unit for As and Pt compositions in equilibrium *mss* is ppm.

c: $PtAs_2$-undersaturated experiment, because the original loaded $PtAs_2$ crystal was completely dissolved into the sulfide.

Table 2 Compositions of each phase in quenched sulfide melts from microprobe analysis (wt%).

Phase	Element	SPT20	SPT17	SPT15	SPT21	SPT16	SPT5	SPT12	SPT3	SPT14	SPT9	SPT10	SPT11	SPT13
q-*iss*	Fe	37.18±0.78	40.03±1.47	36.87±0.53	37.46±0.37	40.43±1.14	34.3±1.07	34.12±2.03	38.07±0.36	37.38±0.42	32.03±2.0	32.42±1.2	35.7±1.14	38.46±0.65
	Ni	2.48±0.80	5.85±1.22	3.4±0.27	3.18±0.28	6.26±1.04	3.1±0.67	3.88±0.22	3.5±0.83	2.1±0.16	4.0±0.6	3.47±0.66	3.7±0.09	2.25±0.23
	Cu	27.98±0.77	21.05±1.93	26.12±0.78	25.74±0.51	17.78±1.49	30.11±0.81	27.51±1.95	23.49±0.39	24.3±0.32	28.8±2.2	28.88±1.63	26.4±0.82	25±0.47
	S	30.62±0.52	32±0.04	31.61±0.41	32.92±0.25	33.04±0.43	31.76±0.88	33.93±0.54	33.09±1.01	35.22±0.16	34.0±0.5	34.03±0.38	33.4±1.64	33.53±0.33
	As	0.032±0.007	0.028±0.01	0.041±0.007	< 80 ppm[a]	0.028±0.006	0.01±0.004	0.046±0.022	0.26±0.155	0.018	0.015±0.008	0.094±0.036	0.062±0.036	0.223±0.045
	Pt	0.046±0.012	0.126±0.025	0.196±0.088	0.158±0.0978	1.385±0.035	0.085±0.034	0.369±0.187	0.67±0.188	0.235±0.04	0.248±0.165	0.25±0.04	0.109±0.015	0.545±0.14
	Total	98.33±0.50	99.21±1.21	98.23±0.5	99.48±0.38	98.91±1.08	99.3±0.75	99.86±0.64	99.07±0.82	99.1±0.51	99.31±0.89	99.02±0.44	99.4±1.21	100±0.67
q-*mss*	Fe	52.68±0.19	53.39±1.57		50.24±0.16	52.10±1.56		32.68±2.73	47.18±0.48	42.08±1.37			30.63±1.31	42.55±1.35
	Ni	7.80±0.28	7.64±0.99		9.85±0.15	8.57±1.03		26.71±1.23	11.26±0.37	17.66±1.26			26.49±1.65	17.87±1.36
	Cu	3.66±0.25	3.69±0.51	q-*mss* is too small to analyze	3.41±0.11	3.34±0.42	q-*mss* is too small to analyze	5.03±1.32	4.57±0.38	3.45±2.38	q-*mss* is too small to analyze	q-*mss* is too small to analyze	9.03±0.64	1.99±0.37
	S	34.78±0.1	32.4±2.77		35.93±0.20	32.4±1.56		35.76±0.113	36.03±0.14	37.5±0.21			34±0.6	37.13±0.11
	As	0.02±0.0075	0.023±0.01		0.012±0.0063	0.017±0.005		0.016±0.004	< 80 ppm[a]	0.137±0.055			0.014±0	0.015±0.0035
	Pt	0.043±0.019	0.071±0.037		0.104±0.031	0.187±0.035		0.419±0.21	0.23±0.0758	0.194±0.083			0.195±0.003	0.557±0.125
	Total	98.97±0.24	97.32±2.24		99.56±0.23	96.62±1.35		100.52±0.12	99.27±0.48	99.96±0.43			100.4±0.36	100.11±0.36
q-BMS-l	Fe	35.82	38.21	35.72±0.0.83		48.43±1.04	33.04±0.74	32.04±2.06	11.27±2.39	36.27±0.94	29.3±1.1	30.1±0.76	31.55±0.7	33.81±0.89
	Ni	8.08	4.26	3.77±0.52		8.09±0.55	6.74±0.43	3.83±0.52	0.88±0.13	2.15±0.22	3.4±0.71	3.45±0.33	3.74±0.04	2.56±0.53
	Cu	23.18	22.89	24.16±1.3		6.43±1.64	27.63±0.86	24.24±0.86	6.51±0.16	20.19±0.62	26.63±0.74	25.15±0.99	25.4±0.71	23.78±0.25
	S	29.35	31.12	30.96±0.29	no q-BMS-l	32.46±2.0	32.86±0.19	30.52±0.47	9.3±1.34	30.20±0.32	30.03±0.88	30.64±0.34	31.8±0.37	31.36±0.54
	As	0.11	0.2	1.47±0.31		0.49±0.12	< 80 ppm[a]	3.59±0.65	33.35±0.11	3.86±0.45	4.00±0.41	4.12±0.85	2.96±0.38	2.7±0.71
	Pt	2.59	2.53	2.44±0.5		1.13±0.42	0.07±0.037	4.42±0.53	43.41±2.86	5.8±0.66	5.48±0.65	5.1±0.19	4.2±0.05	3.7±0.41
	Total	99.13[b]	99.21[b]	98.52±0.34		97.03±1.25	100.33±0.23	98.64±0.30	104.7±1.05[c]	98.5±0.78	98.81±1.05	98.6±0.4	99.6±0.18	97.9±0.72
As droplet	Fe	7.22±1.72	3.09±0.77		2.98±0.99		27.69±0.57		9.11±0.67	14.91				
	Ni	17.82±0.15	11.51±0.83		2.51±1.19		2.45±0.4		0.81±0.03	6.27				
	Cu	4.47±0.39	4.59±0.14		2.4±0.23		24.31±0.65		5.72±0.95	1.58				
	S	0.22±0.04	0.10±0.014	As droplet is < 1 mm	0.224±0.05	As droplet is < 1 mm	24.94±0.29	no As droplet	6.87±2.1	14.83		no As droplet		
	As	18.78±0.63	21.6±1.07		26.8±2.02		0.038±0.012		31.52±2.71	25.14				
	Pt	52.63±0.16	61.08±0.72		66.07±2.21		21.58±0.47		49.52±5.78	37.28				
	Total	101.13±0.66	101.97±0.86		101±1.71		101.01±0.26		103.5±0.6	100.01[b]				

a: The As concentration is below the detection limit of 80 ppm.
b: Most quenched base metal sulfide liquids or quenched As droplets in this sample are too small, only one analysis was done.
c: This is composition of quenched $PtAs_2$ crystal in SPT3.
q-*iss*, quenched *iss*; **q-*mss***, quenched *mss*; **q-BMS-l**, quenched base metal sulfide liquid rich in As and Pt.